Universidade de Coimbra

Solar filaments: Characteristics and Evolution

Master Thesis in Astrophysics and Space Instrumentation

by Ricardo Jorge Maranhas Gafeira

Supervisors
Dr. João Manuel de Morais Barros Fernandes
Dr. Jean Aboudarham

October 10, 2011

Acknowledgments

Ao longo destes anos muitas pessoas contribuíram para a minha evolução tanto académica como pessoal de diferentes maneiras. Evolução essa que me levou até a realização deste trabalho e o meu agradecimento a todas elas. Não posso contudo deixar de agradecer especialmente a algumas pessoas que contribuíram de uma forma especial. Quero agradecer especialmente:

Ao meu orientador em Coimbra, o Professor João Fernandes pela orientação, concelhos e grande ajuda na elaboração deste trabalho.

I would like to thanks to my supervisor in the Paris Observatory, the Dr. Jean Aboudarham, for the support and supervision during my stay at the Paris Observatory and during the thesis work. At the Paris Observatory for hosting me. To Xavier Bonnin, to Christian Reni, and Nicholas Fuller in aid delivery.

Aos meus pais Francisco e Graça, por serem os melhores pais do mundo que sempre me apoiaram nos bons e maus momentos, e por me permitirem as melhores condições durante os meus anos de estudo.

Ao meu irmão Tiago pela amizade, companheirismo e por estar sempre presente quando eu precisei ao longo destes anos.

À Joana pela grande amizade e cumplicidade.

Ao Professor Nuno Peixinho pela ajuda durante a elaboração deste trabalho e pelos precisos conselhos.

À Professora Alexandra Pais pela ajuda na elaboração desta

tese.

Ao Senhor Aquiles, à Senhora Virginia, à Clarisse e a Solene pela amizade e por tudo o que fizeram por mim durante a minha estadia em Paris.

À Dr. Adriana Garcia e a Senhora Dora Duarte, pelo acolhimento e simpatia nos periodos que passei no Observatório Astronómico de Coimbra.

Aos meus amigos Tiago, Borda Vieira, Carina, Pedro Silva, Pedro Melo, Mamede, Nuno, Susana, Martins, Marcio, Rosado, Jegundo, Silvia entre muitos outros por todos os tempos passados dentro da aulas, pelos tempos passados na vida associativa e pelos momentos de diversão.

À Unidade 405 - Centro de Física Computacional da Universidade de Coimbra pelo apoio financeiro através da bolsa de iniciação cientifica.

Resumo

Este trabalho tem como principal objectivo o estudo dos filamentos solares, começando com um estudo estatístico que levou à criação e implementação de um modelo computacional.

Os estudos estatísticos realizados estão relacionados com a longitude e latitude de Carrington, com o comprimento, a curvatura e a orientação dos filamentos. Durante a realização do estudo estatístico referente à orientação levantou-se a necessidade da elaboração do simulador.

O simulador permitiu-nos verificar que as alterações na distribuição da orientação observada eram causadas por efeitos de perspectiva. Outro elemento de interesse que podemos extrair do simulador é a distribuição da orientação de aparecimento dos filamentos, distribuição esta que até à data, tanto quanto pude verificar na bibliografia, não foi alvo de publicação.

Abstract

This work has as main objective the study of solar filaments, starting with a statistical study that led to the creation and implementation of a computational model.

The statistical studies performed are related to the Carrington longitude and latitude, the length, curvature and orientation of the filaments. In carrying out the statistical studies related to the orientation we needed to make the simulator.

The simulator allowed us to verify that the changes observed in the distribution of orientation were caused by perspective effects. Another interesting element that we can extract is the distribution of orientation appearance of the filaments, that by the research in the literature that I did, was not published yet.

Contents

1 Introduction **1**

1.1 The solar structure: A brief summary 2

1.1.1 Photosphere 5

1.1.2 Chromosphere and Corona 10

1.2 Filaments 14

2 Statistic study of filaments behavior **23**

2.1 Data acquisition, and data handling. 24

2.1.1 Spectroheliograph 24

2.1.2 Automatic detection 25

2.1.3 HFC database 30

2.2 Carrington longitude preferential zones 32

2.3 Carrington latitude of filament skeleton center 34

2.3.1 Observation 34

2.3.2 Drift 35

2.4 Length of the filament 38

2.5 Curvature 40

2.6 Correlation between active regions and filaments. 43

2.7 Orientation of filaments 45

3 Simulation **49**

4 Conclusion and perspectives **67**

List of Figures

1.1 Global structure of the sun. (http://www.nasa.gov) 2
1.2 Rotation of plasma around the solar axis. [2] 4
1.3 (Left panel)Representation of convective cells as seen from the top (ttp://frigg.physastro.mnsu.edu). (Right panel) Scheme of the convective zone. 4
1.4 Zeeman effect for one sunspot. The right side of the image is the spectrum of the vertical black line showed in the left side of the image. There, we see the splitting of the spectral lines caused by the intense magnetic field. Note that as more intense the field, the splitting increases (http://eo.nso.edu). . . 5
1.5 Representation of one sunspot. In the centre the dark umbra surrounded by the penumbra (http://sandcarioca.wordpress.com). 6
1.6 (Right panel) Example of the inclination of a pair of sunspots and active regions [3].(Left panel) Plot of the inclination in function of latitude. 7
1.7 Image of a pore (black zone in the center of the image) (http://www.mps.mpg.de). 7
1.8 (Top panel) Butterfly diagram where is represented the variation of latitude of sunspots with time. (Botton panel)Average daily sunspot area in % of visible hemisphere. (www.nasa.gov) 8
1.9 (Left image) Solar faculae. (Right image) Variation of the radiation flux during time (Nature 443, 161-166). 9
1.10 Density and temperature of the chromosphere and corona. Adapted from (Cambridge Encyclopedia of the sun). 10

1.11 Photograph of the sun where we observe the coronal holes (http://hfradio.org). 11
1.12 Photograph of the sun, where we observe the mass ejection (http://www.cosmiclight.com). 12
1.13 Photograph of the sun, where we observe a coronal solar flare- (http://astropt.org). 12
1.14 Photograph of the sun, where we observe a solar prominence (http://2.bp.blogspot.com). 13
1.15 Image of the sun obtained using a $H\alpha$ filter where the dark filaments are observed (Observatory of Paris). 14
1.16 Filaments observed on 1 May 2002 in $H\alpha$ radiation at the Paris observatory, filaments in black and the inversion line are the solid lines [8]. 19
1.17 Two possible fields topologies. The solid lines are the magnetic field and the central rectangle represents the filament. The left panel represent the normal polarity (N-type) and the right panel represents the inverse polarity (I-Type). 19
1.18 Simulation of a filament created by an active region where we see the coronal arcades and inside them the magnetic field lines belonging to the filaments [9]. 20
1.19 The zone between the long white arrows is the middle of an empty filament channel. This image was recorded at the Big Bear Solar Observatory. 21
1.20 Sketch of chirality definition. 21

2.1 Scheme of the spectroheliograph of the University of Coimbra Observatory [12]. 24
2.2 Scheme of the angle θ is measured. 27
2.3 Segmentation results for the 1st of April 2001, 08:45:00 UT: (a) original Hα image from Meudon, (b) seeds detected, (c) region growing results and (d) original and results superimposed [13]. 28
2.4 Filament skeleton (white line) superimposed on the original image [13]. 29

2.5 Histogram with bin size of 1 of Carrington longitude for 5 days. 32
2.6 Histogram with bin size of 1 of the Carrington latitudes of the observed filaments and best fitted curve with two gaussianans. 34
2.7 Plot of the mean values of the gaussian for each hemisphere and the respective linear fit. 36
2.8 Data obtained for the mean of the various gaussian fitting for the latitude for each Carrington rotation. In this plot are also shown the fitted curves given by equation 2.9. 38
2.9 Histogram with bin size of 1 of the length of the filaments skeleton. 39
2.10 Histogram with bin size of 0.1 of the curvature index of filaments along the whole cycle. 40
2.11 Data for the decay factor, obtained from the fitting of equation 2.11 to the curvature for each Carrington rotation. In this plot is also shown the curve fitted to the data using equation 2.12. 42
2.12 The top panel is the histogram with bin size of 1 of the latitude of the filaments skeleton center in the year 1999. The down panel is the same histogram but for the active regions center. . 44
2.13 Scheme showing how the orientation angle is measured relative to the equator line. 45
2.14 Number attributed to each quadrant. 45
2.15 Histogram with bin size of 1 of orientation of filaments per quadrant. Top right panel correspond to the first quadrant. Top left panel correspond to the second quadrant. Down left panel for the third quadrant. Down right panel for the fourth quadrant. 46
2.16 Number attributed to each "octant". 47
2.17 Histogram with bin size of 1 of the orientation of filaments per "octant". 48

3.1 NCDF obtained for the latitude appearance of filaments skeleton centre. 50
3.2 NCDF obtained for the length of filaments skeleton. 51

3.3 Example of the results obtained when the *sinus* shape are considered and using the parameters values of table 3.1. The blue line is the observable data, the black line is the result of the simulation and yellow and red lines are the simulation result± 2σ. 58
3.4 Example of the evolution in time of four simulated filaments. . 59
3.5 Flowchart of the simulation program. 60
3.6 Distribution of initial orientation distribution obtained using the parameters inside the table 3.1. Right panel is the lateral view and the left panel is the top view. 61
3.7 NCDF of initial orientation distribution showed in figure 3.6. . 61
3.8 Results of the simulation obtained using the parameters inside the table 3.1. The blue line is the observed result the black line the result of the simulation and yellow and red lines are the simulation result± 2σ. 62
3.9 Example of parameters that produce bad results. a_1=0.1, b_1=2, c_1=0.01 , d_1=0.7, a_2=2, b_2=4, and c_2=0.01. The blue line is the observable result the black line the result of the simulation and yellow and red lines are the simulation result± 2σ. 63
3.10 Result obtained using the parameter inside the table 3.1 except the parameter d wich is equal to 0. The blue line is the observable result the black line the result of the simulation and yellow and red lines are the simulation result± 2σ. 64
3.11 Example of the results obtained when we consider a criation of the filaments with a unique orientation $\pi/8$. The blue line is the observable result the black line the result of the simulation and yellow and red lines are the simulation result± 2σ. 65
3.12 Example of the formation of the filaments between two active regions [21]. 66

List of Tables

2.1 Tables in the HFC 30
2.2 Description of the VIEW_FILAMENTS_FULL table. The information inside this table is extracted from the automatic detection program [13]. 31
2.3 Values obtained for the parameters of equation 2.8 by fitting two gaussians to the data showed in figure 2.6. The corresponding curve is showed in the same plot. 35
2.4 Slopes obtained by the linear fitting the data for Carrington latitude of filaments for each Carrington rotation during all cycle. The slope is in deg/CR. 37
2.5 Values obtained for the parameters of equation 2.9 when fitting the data showed in figure 2.8. The fitted curves are shown in the same plot. 37
2.6 Values obtained for the parameters of equation 2.12 by fitting it to the data showed in figure 2.11. The corresponding curve is shown in the same plot. 41

3.1 Parameters inside the equations 3.2 and 3.3 by this procedure that produce the best agreement between observed and simulated data. 55
3.2 Differences in percentage of the parameter used in figure 3.8 and in figure 3.9. 55

List of acronyms

HFC - Heliophysics Feature Catalogue

HELIO - Heliophysics Integrated Observatory

CCD - Charge-Coupled Device

FITS - Flexible Image Transport System

PNG - Portable Network Graphics

BMP - Bitmap Image File

NCDF - Normalized Cumulative Distribution Function
CR - Carrington Rotation

Chapter 1

Introduction

The structure of this thesis is constructed to introduce the reader to the sun in general where the different zones of the sun and the solar phenomena are described in a global form. After this general description a more detailed study about the solar filaments is showed in such a way as to give a more solid background about this phenomena that is the core of this work.

The study of the different behaviors of the solar filaments is very important because we can extract a lot of information that can be used in the study of the solar magnetic field. In order to do this we made the statistical study from where I extract information from different behaviors of filaments and try to give an explanation of then based, if applicable, on the solar magnetic field.

Another point is the simulator described in chapter 3 that was created during the work of this thesis to solve the difficulties of the interpretation of the observable orientation.

This simulation is a crucial point of this thesis because, based on the publications on this field that I read, it's the first time that a simulation of this type is built in part because is the first time that the information inside the HFC database is obtained. In my point of view the two most important achievements of the simulation are: it gives explanation about the behavior of the observable orientation; and give us the distribution of orientation of appearance of the filaments that is not published yet.

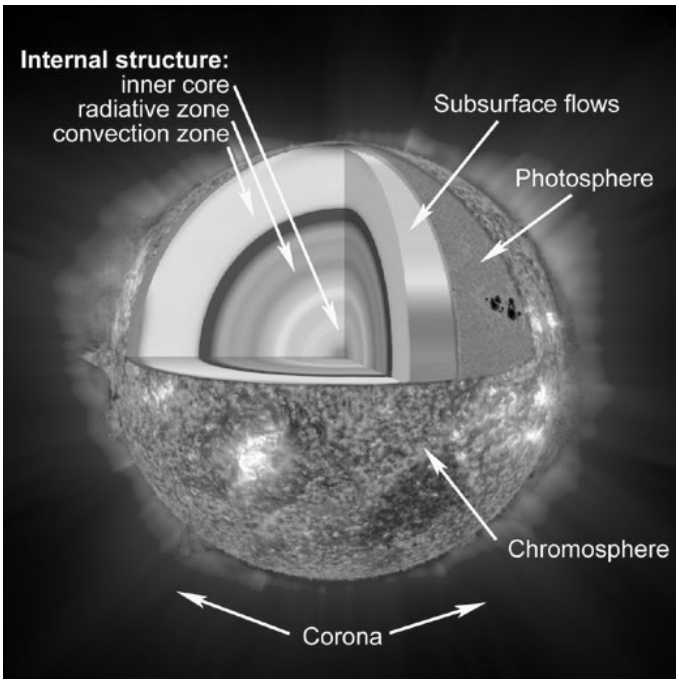

Figure 1.1: Global structure of the sun. (http://www.nasa.gov)

1.1 The solar structure: A brief summary

In this section we refer to the global solar structure from the most internal to the most external zone of the sun. Traveling from the interior to the exterior passing through every zone, we will point out the most important observable phenomena that occur there.

We will start to show a global view of the sun.

In figure 1.1 we see the most interior structure of the sun, the core. It has a radius of $\approx 0.2R$, where R is the sun's radius. Nuclear fusion occurs here and the energy released by this process is the main source of energy for all the sun. For the study that we are going to make, the core does not have any particular interest.

The next structure of the sun is the radiative zone. Here, the transport of energy is made only by radiative propagation. The upper limit is defined by the Schwarzschild criteria, that fixes the limit of the existence of convection.

Convection exists if,

$$\nabla - \nabla_{ad} > 0 \tag{1.1}$$

where,

$$\nabla = \frac{d \ln T}{d \ln P} \ , \tag{1.2}$$

∇_{ad} is the adiabatic gradient, T is the temperature and P the pressure [1]. So if the condition 1.1 is not verified convection does not exist, which is the case of the radiative zone. The radiative zone rotates like a rigid body, with period of ≈ 27.3 *days* [2].

Between the radiative zone and the convective zone, there are two layers with distinct characteristics, the overshoot and the tachocline. The overshoot zone is related to the interface between an environment where doesn't exist convection and an environment where convection exists. In this zone operates a semi-convection regime, due to the buoyancy force acting on the plasma that falls from the convective zone and is heated again by radiation from the radiative zone.

The other boundary zone, is the tachocline. This zone is the boundary between a region where the plasma rotation around the solar axis is like a rigid body (the radiative zone) and a region with differential rotation of the plasma (the convective zone). In figure 1.2, is shown the rotation of the plasma around the axis in the solar radiative zone and in the convective zone. The tachocline is in between.

The convective zone is characterized by the fact that the energy transport is done mainly by convection. In this region there is also radiative transport but the convective component is dominant. Figure 1.3 represents the convective cells which are responsible for transporting energy.

In figure 1.2 we can see that there are three zones with different rotation rates. For latitudes between 0 and 15 degrees, the rate is higher than the global sun rotation rate, between 15 and 45 the rotation rate is close to the rotation rate of the radiative zone and for higher latitudes than 45 the rotation rate of the plasma is lower than the other two zones. The differences in rotation rates between different zones is called differential rotation [2].

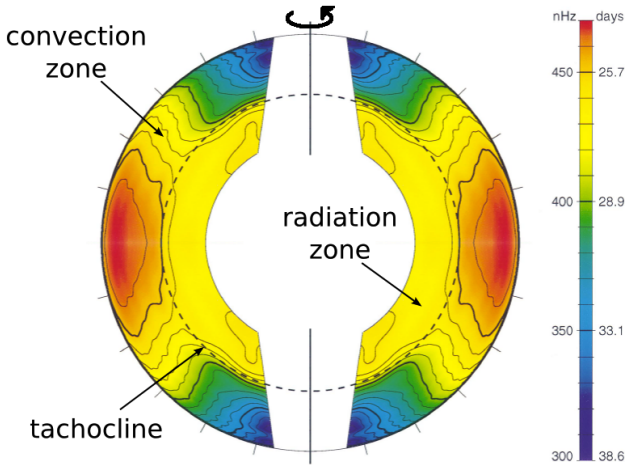

Figure 1.2: Rotation of plasma around the solar axis. [2]

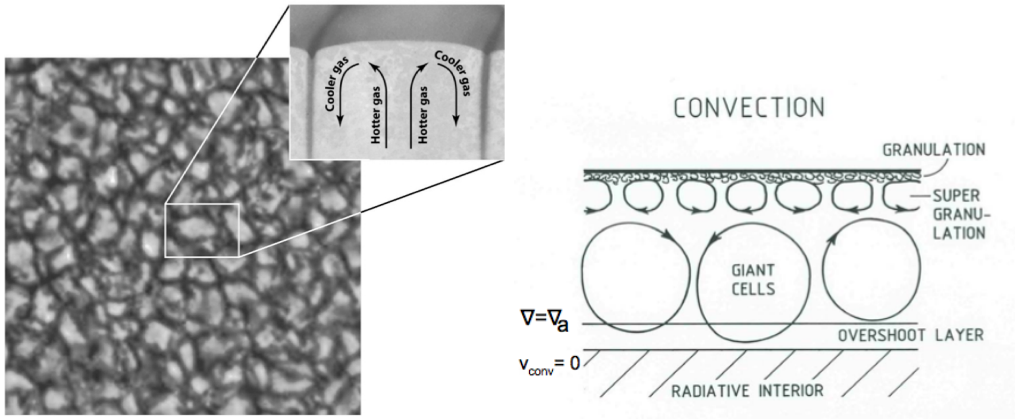

Figure 1.3: (Left panel)Representation of convective cells as seen from the top (ttp://frigg.physastro.mnsu.edu). (Right panel) Scheme of the convective zone.

1.1.1 Photosphere

Near to the surface of the sun, the plasma begins to become transparent to visible radiation,this can be described by the optical depth which in the photosphere has the value of 2/3 [1]., and we start being able to observe this region and its phenomena and properties.

Through the Zeeman effect we see that there exists a strong relationship between the solar magnetic field and solar phenomena. In figure 1.4 we see this effect for one sunspot where the different spectral lines are split by the magnetic fields.

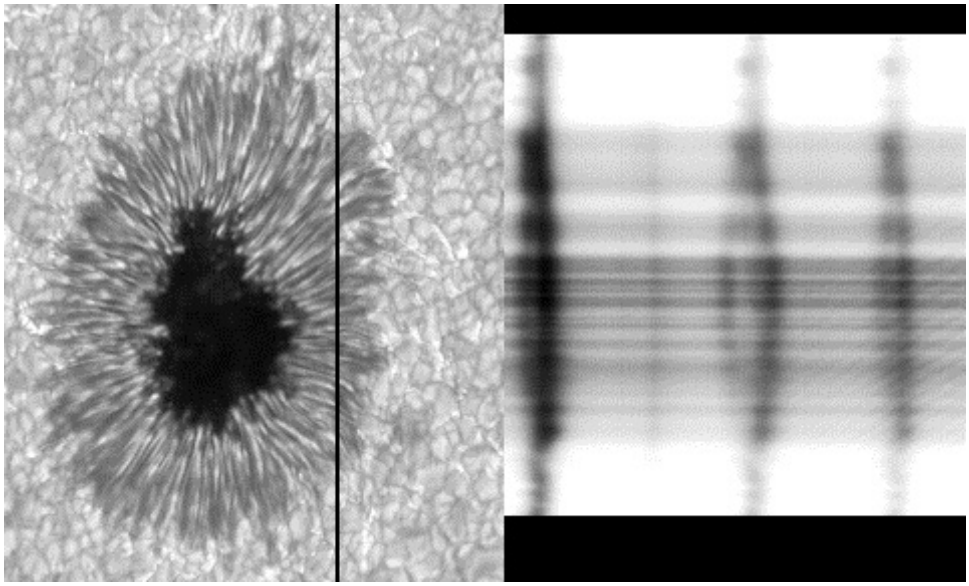

Figure 1.4: Zeeman effect for one sunspot. The right side of the image is the spectrum of the vertical black line showed in the left side of the image. There, we see the splitting of the spectral lines caused by the intense magnetic field. Note that as more intense the field, the splitting increases (http://eo.nso.edu).

The first phenomena that I will describe are the sunspots. The sunspots are darker and more cool areas on the surface of the sun. Within them we can identify two distinct zones, the penumbra and the umbra. The umbra is the central, darkest zone of the sunspots. The magnetic field is intense ($\approx$3000G) and the temperature is around 4000K. Here, the magnetic field is

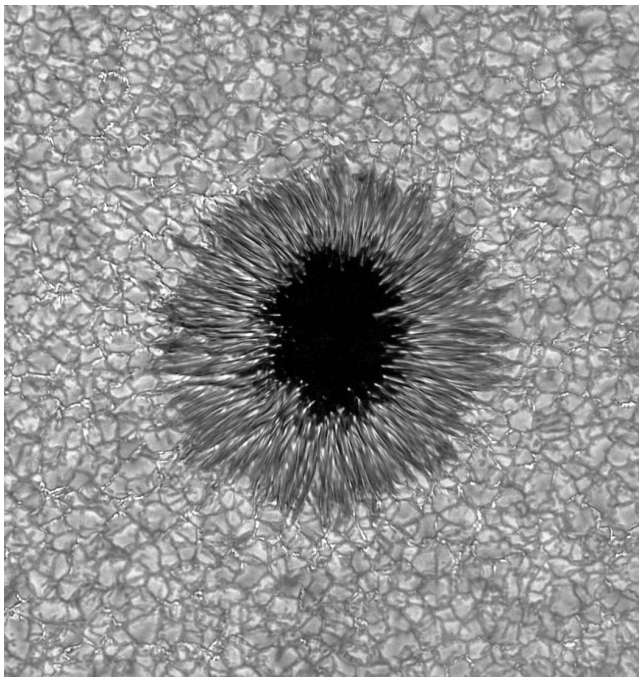

Figure 1.5: Representation of one sunspot. In the centre the dark umbra surrounded by the penumbra (http://sandcarioca.wordpress.com).

nearly perpendicular to the surface of the sun.

The penumbra is the transition zone between the umbra and the quiet surface of the sun. The magnetic field there reaches ≈2000G, and is more inclined than in the umbra. Its temperature is about ≈5000K. Penumbra present a filamenteous structure composed by hotter plasma coming from the sun interior and more cold plasma, which is trapped by the magnetic field.

In figure 1.5 is represented one sunspot. It is rare the appearance of a single sunspot. Usually on the photosphere they appear in couples, inside active regions [1] where magnetic field lines connect the sunspot couples. This couples of spots have opposite polarity between them, have an interesting characteristic that is their inclination to the sun equator, which increases as far as they are from the equator, as show in figure 1.6. Sometimes, active zones appear as being identical to sunspots but without penumbra. These phenomena are called pores, as the one shown in figure 1.8.

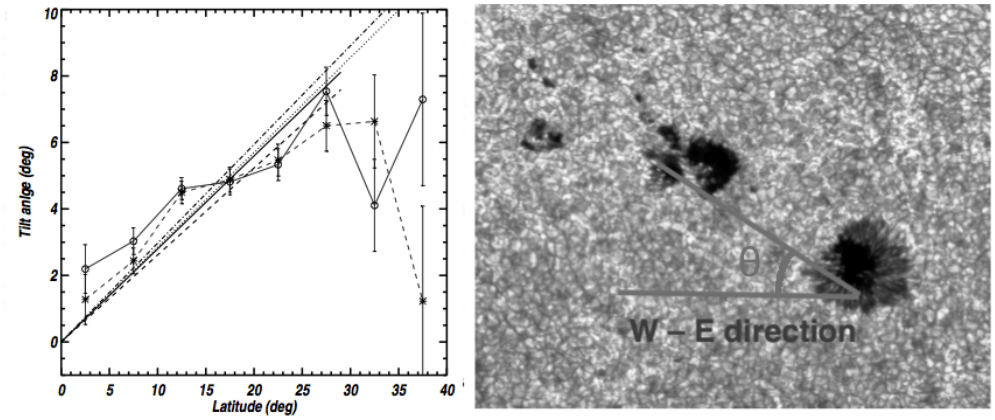

Figure 1.6: (Right panel) Example of the inclination of a pair of sunspots and active regions [3].(Left panel) Plot of the inclination in function of latitude.

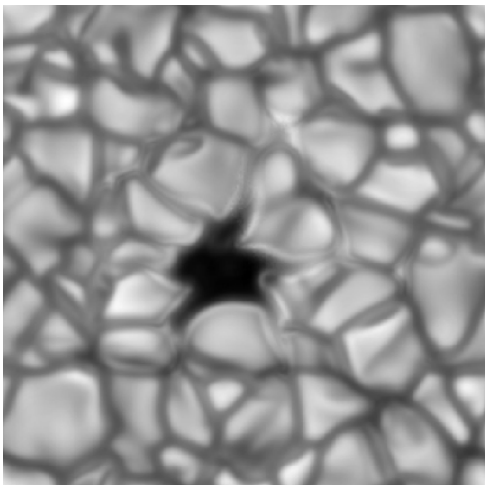

Figure 1.7: Image of a pore (black zone in the center of the image) (http://www.mps.mpg.de).

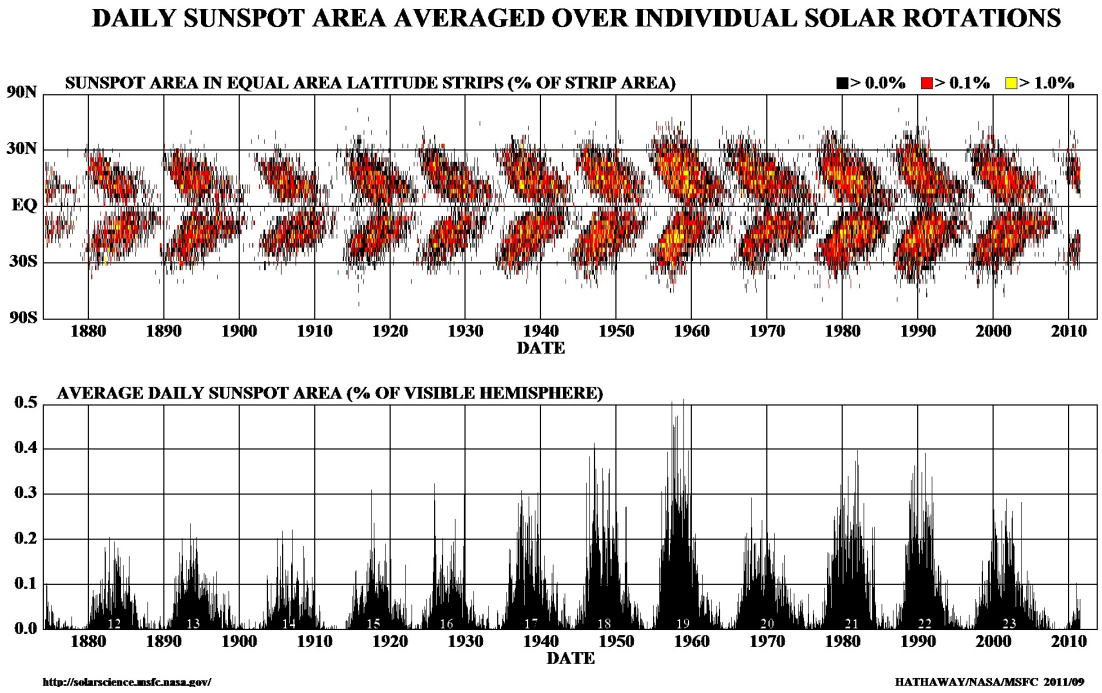

Figure 1.8: (Top panel) Butterfly diagram where is represented the variation of latitude of sunspots with time. (Botton panel)Average daily sunspot area in % of visible hemisphere. (www.nasa.gov)

Plotting the latitude of the sunspot in function of time, we see aggregates looking like butterfly wings along the solar 11 years cycle, producing the called butterfly diagrams as shown in figure 1.8. In this diagram we see also a migration of sunspots from higher latitudes at the beginning of the cycle, down to latitudes closer to the equator at the end of the cycle. Another characteristic behavior that is visible in figure 1.8 is the appearance of larger sunspot areas, represented by yellow dots near the solar maxima.

Finally we still need to refer the solar faculae. The faculae are bright and hot zones in the solar surface, like those shown in figure 1.9. They are present at all times of the solar cycle not only at the maximum as with sunspots. But their number is much higher during the maximum activity. The faculae are responsible for the increase of radiation flux of the sun during the solar maximum, when the existence of a high number of darker sunspots

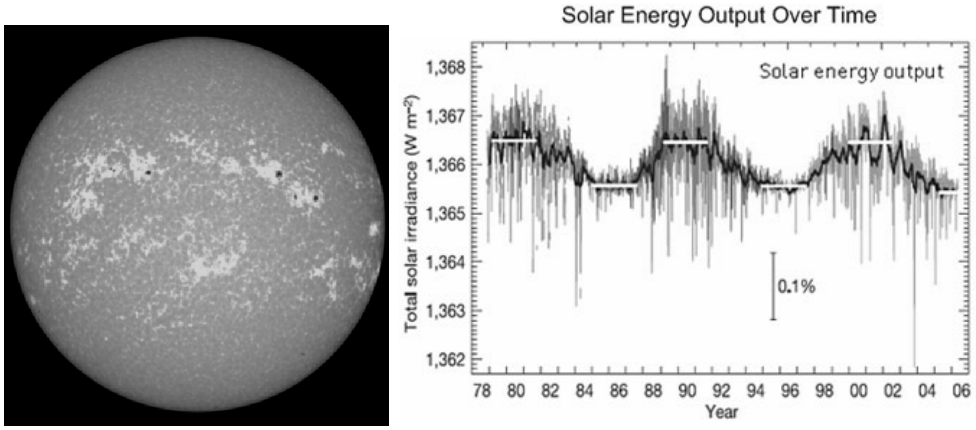

Figure 1.9: (Left image) Solar faculae. (Right image) Variation of the radiation flux during time (Nature 443, 161-166).

was expected to decrease the flux. But the increasing number of faculae counteracts this effect, leading to an increase in total luminosity of the sun, as shown in figure 1.9.

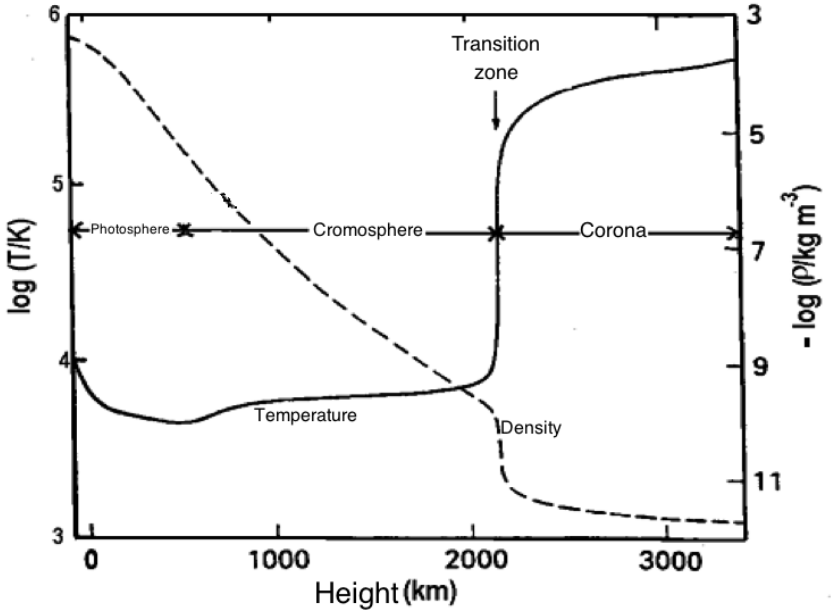

Figure 1.10: Density and temperature of the chromosphere and corona. Adapted from (Cambridge Encyclopedia of the sun).

1.1.2 Chromosphere and Corona

In this section we will refer the two outer layers of the sun. The chromosphere and the corona.

The chromosphere is characterized by a large decrease in plasma density and a small increase in temperature. Between the chromosphere and the corona, there is a transition zone characterized by a sudden decrease in density and a sudden increase in temperature. In the corona the density decreases a little bit and the temperature increases to values of the order of magnitude of a million kelvins. This behavior is represented in figure 1.10.

In the corona, we can find some more solar phenomena. One of this phenomenon is the coronal holes, shown in figure 1.11. This phenomena is characterized by the disappearance of plasma from the corona originating these holes that are observed as black areas. Sometimes, plasma is ejected from the corona and carries along some magnetic field lines. These mass ejections can be divided into two classes, the CME (coronal mass ejections) and solar flares. The CME are a relatively slow ejection of plasma sometimes

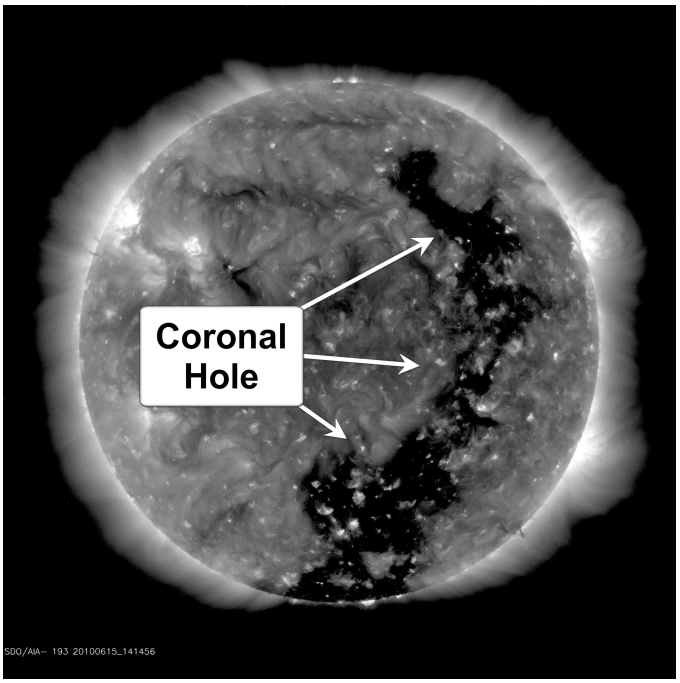

Figure 1.11: Photograph of the sun where we observe the coronal holes (http://hfradio.org).

arc-shaped, as in figure 1.12. The solar flares are much more energetic ejections with very high plasma velocity like an explosion. In figure 1.13 we see one bright spot where one solar flare is starting.

Another kind of solar event that can occur in the chromosphere and in the corona is the prominence. The solar prominences are structures of more cold and dense plasma than the chromosphere and corona average values, they are supported through the intense magnetic fields.

These prominences are visible as arc-shaped structures outside the solar limb, as shown in figure 1.14. When the prominences are observed inside the solar disc, what we see is the projection of the arc in the solar surface. We then observe linear structures, that are called filaments. These filaments are the object of the present study.

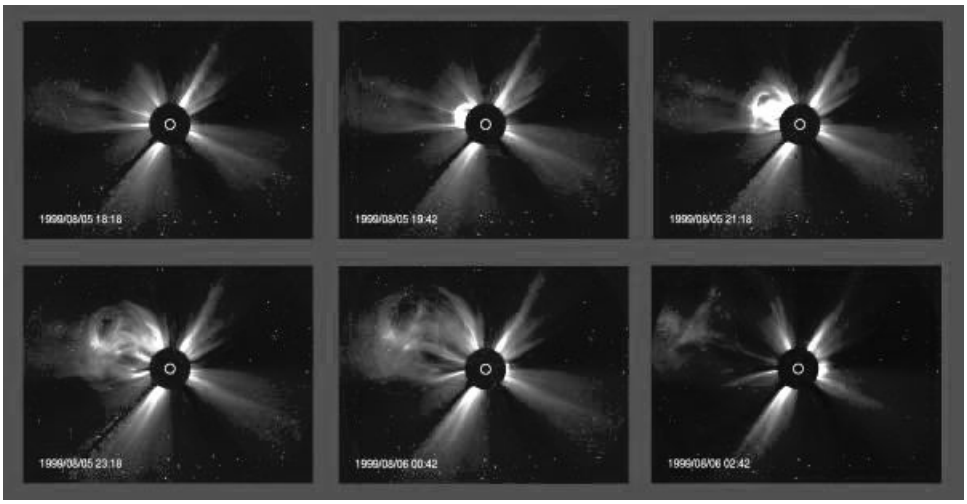

Figure 1.12: Photograph of the sun, where we observe the mass ejection (http://www.cosmiclight.com).

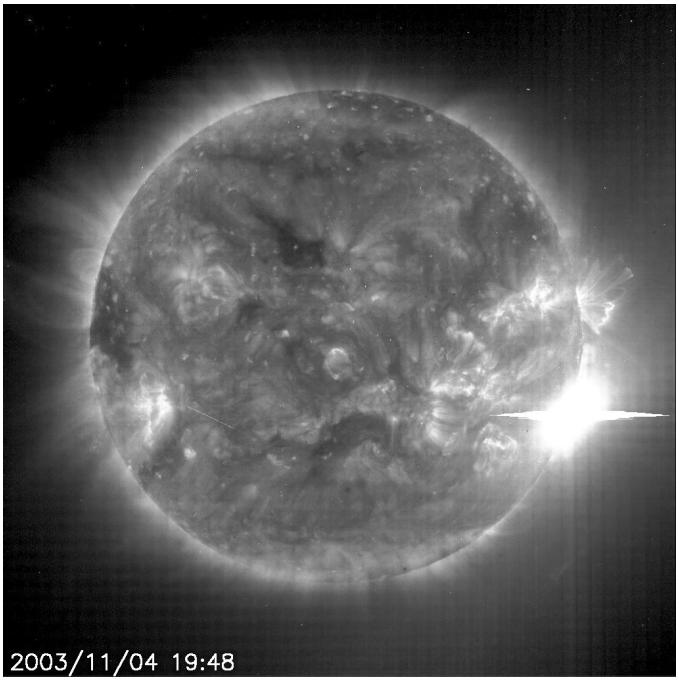

Figure 1.13: Photograph of the sun, where we observe a coronal solar flare-(http://astropt.org).

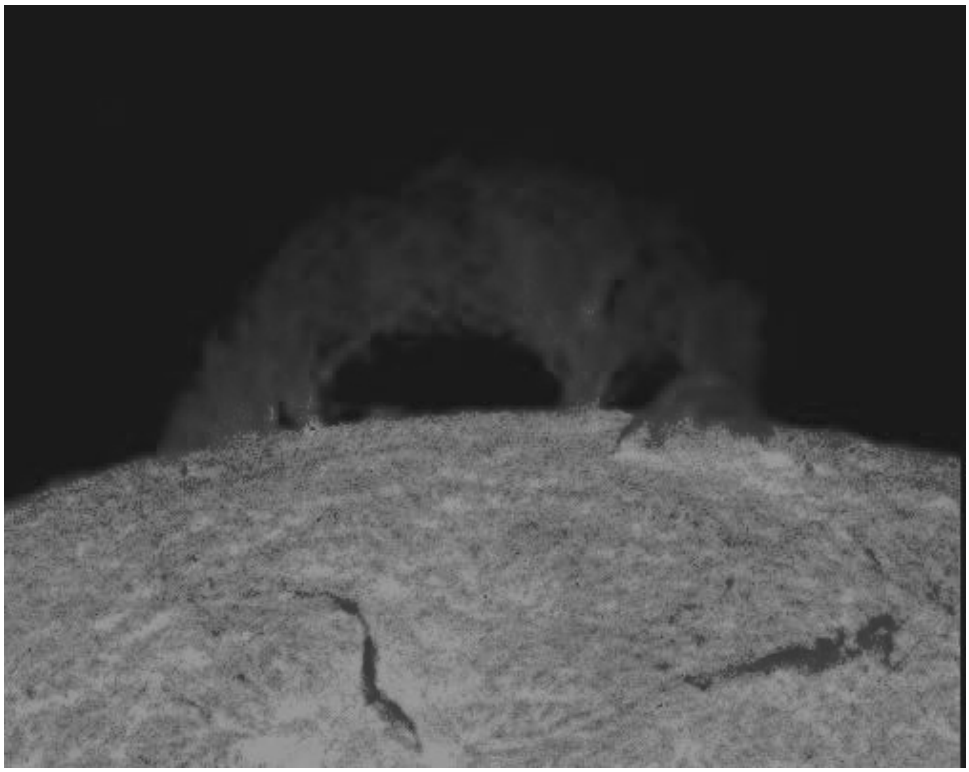

Figure 1.14: Photograph of the sun, where we observe a solar prominence(http://2.bp.blogspot.com).

1.2 Filaments

In this section we describe in more detail the structure and characteristics of solar filaments.

How does a filament look like? When we observe the sun using filters that allow to observe the chromosphere, the filaments appear like elongated dark structures on the solar disk because they absorb the chromosphere light . Figure 1.15 is a spectrogram of the sun obtained using ($H\alpha$) filter 656.28 nm where the filaments are visible. The dark arrow indicates the position of one of these.

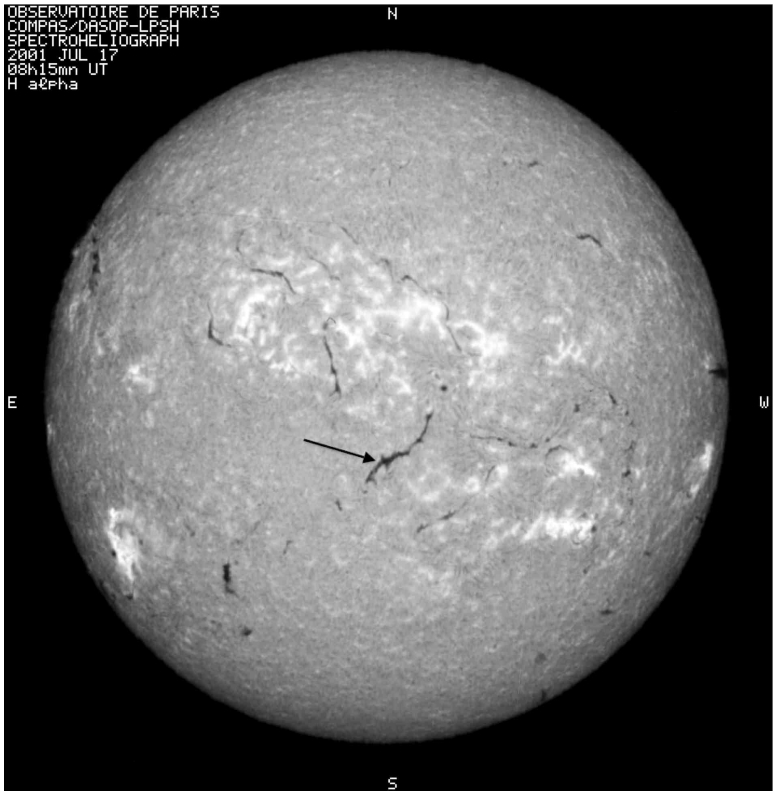

Figure 1.15: Image of the sun obtained using a $H\alpha$ filter where the dark filaments are observed (Observatory of Paris).

As already said, the filaments consist in cold and dense plasma comparing to the external environment. Due to this, they appear dark because they absorb the light coming from the chromosphere.

The equation of energy which is appropriate for the optically thin corona is [4],

$$\frac{\rho^\gamma}{\gamma - 1}\frac{D}{Dt}\left(\frac{p}{\rho^\gamma}\right) = -\nabla \cdot (\kappa \nabla T) - \rho^2 Q(T) + \frac{j^2}{\sigma} + h\rho \tag{1.3}$$

where γ is the adiabatic index, ρ is the plasma density, p the hydrostatic pressure, κ is the thermal conductivity, $Q(T)$ is the optically thin radiative loss function, j is the electric corrent, σ the electrical conductivity, and h represents the coronal heating rate per unit mass and can be obtained for the coronal plasma assuming that is constant. The right side of the equation 1.3 comprises the contributions of thermal conduction, optically thin plasma radiation, ohmic heating and the small-scale heating term.

The cooling function at constant gas pressure and neglecting conduction is,

$$\frac{Q(T)}{T} = \frac{k_B h}{pm} \tag{1.4}$$

where k_B is the Boltzmann constant and m the mean atomic mass.

Applying equation 1.3 to the corona considering that σ is $>>$ 1 and h is $<<$ 1 we obtain,

$$C_p \frac{\partial T}{\partial t} = \rho Q(T) + \frac{\kappa}{\rho}\frac{\partial^2 T}{\partial s^2} \tag{1.5}$$

where s is the distance along the magnetic field line.

Now we introduce the variations [5] $T = T_0 + T_1$ and $\rho = \rho_0 + \rho_1$ to the system and the using equations 1.18 and 1.5 obtain,

$$C_p \frac{\partial T_1}{\partial t} = \frac{\rho_0 Q(T)}{T_0} T_1 + \frac{\kappa}{\rho_0}\frac{\partial^2 T_1}{\partial s^2} \tag{1.6}$$

Assume now that the perturbation vanishes at the end of the magnetic line, of length L, the T_1 can be taken proportional to $exp(\omega t + 2\pi i s/L)$,to ensure that the temperature at the ends of the filament is equal to the corona, and equation 1.6 reduces to,

$$\omega = \frac{\rho_0 Q(T)}{T_0 C_P} - \frac{\kappa}{\rho_0}\frac{4\pi^2}{L^2 C_P} \tag{1.7}$$

From equation 1.7 we can determine the maximum length, L_m, of the magnetic structure where the plasma becomes thermally unstable.

$$L_m = 2\pi \left[\frac{\kappa T_0}{Q(T)\rho_0^2}\right]^{1/2} \tag{1.8}$$

When L_m is exceeded, the plasma becomes thermally unstable and cools down until a new equilibrium is reached and a prominence has formed like condensation [6].

But how the filament is supported by magnetic forces! We start to introduce the induction equation [7].

$$\frac{\partial \mathbf{B}}{\partial t} = \nabla \times (\mathbf{v} \times \mathbf{B}) + \eta \nabla^2 \mathbf{B} \tag{1.9}$$

Where B is the magnetic field, v the velocity field and η is the magnetic diffusivity. The magnetic diffusivity is given by $\eta = (\mu\sigma)^{-1}$ where μ is the magnetic permeability, and σ is the conductivity of the medium. This equation shows that the time evolution of the magnetic field is caused by the movement of plasma relatively to $\mathbf{B}$ (first term on the right side of the equation) and by the diffusion of magnetic field (second term on the right side of the equation). The ratio between the magnitudes of the first and second terms is called the magnetic Reynolds number and is defined by,

$$R_m = \frac{v_0 l}{\eta} \tag{1.10}$$

where v_0 and l are respectively a characteristic velocity and length of the system. If $R_m >> 1$ the plasma flow dominates and the field is frozen to the plasma. If $R_m << 1$ the diffusion dominates the evolution of the magnetic field.

The magnetic force (Lorentz force) is given by,

$$\mathbf{j} \times \mathbf{B} = -\nabla\left(\frac{\mathbf{B}^2}{2\mu}\right) + \frac{(\mathbf{B}.\nabla)\mathbf{B}}{\mu} \tag{1.11}$$

and the first term of the right side of equation represents a force created by the difference of magnetic field between two regions where $\frac{B^2}{2\mu}$ is a magnetic pressure, and the second term on the right side of equation is the magnetic tension force acting towards the centre of curvature of curved magnetic field lines.

The parameter that relates the hydrostatic pressure and the magnetic pressure is β and is defined by,

$$\beta = \frac{p}{\mathbf{B}^2/(2\mu).} \tag{1.12}$$

We can see if the medium is characterized by $\beta << 1$, the magnetic pressure dominates (high magnetic fields) and where $\beta >> 1$ the hydrostatic pressure is the dominant term.

The fluid equation of motion is given by,

$$\rho\frac{D\mathbf{v}}{Dt} = -\nabla p + \mathbf{j} \times \mathbf{B} + \rho\mathbf{g} \tag{1.13}$$

where g is the gravity. From the analysis of this equation we see that the plasma is acted by a pressure gradient, the magnetic force and by gravity acceleration.

Considering that the filaments are in equilibrium under a balance between different forces, where the plasma flow speed is much smaller then the sound speed,

$$v_S = \left(\frac{\gamma p}{\rho}\right)^{1/2} \tag{1.14}$$

, the Alfvén speed,

$$v_A = \frac{B}{(\mu\rho)^{1/2}} \tag{1.15}$$

and the free-fall speed, then equation 1.13 reduces to,

$$0 = -\nabla p + \mathbf{j} \times \mathbf{B} + \rho\mathbf{g}. \tag{1.16}$$

Consider now a case where the magnetic field is axial, then the magnetic force is perpendicular to the field, implying that the force does not have a component along the z axis. In this case equation 1.16 along the z component reduces to.

$$0 = -\nabla p - \rho g \tag{1.17}$$

Using the ideal gas law,

$$\rho = \frac{mp}{k_B T} \tag{1.18}$$

we can reduce equation 1.17 to the integral form eliminating ρ,

$$p = p_0 \; exp\left(-\int_0^z \frac{dz}{\Lambda(z)}\right) \tag{1.19}$$

where $\Lambda(z) = \frac{k_B T(z)}{mg}$ is the pressure scale-height. Typically in the corona is 10^5 km.

Assuming that the temperature is uniform equation 1.19 becomes,

$$p = p_0 exp\left(\frac{-z}{\Lambda}\right) \tag{1.20}$$

where we see that the pressure decreases exponentially with height along each magnetic field line (we assume $\mathbf{B} = B_z\hat{k}$).

When the filament cools, becomes more dense and tends to go to lower heights, thereby curving magnetic field lines like figure 1.17 show. This perturbation of the magnetic field lines increases the importance of the second term on the right side of equation 1.11. The balance between this force the impulsion force and gravity it is what keeps the filament stable.

The zones where magnetic field possibly has the properties to support the filaments is called neutral lines of magnetic field [8], figure 1.16.

These lines are characterized as being the zones where the radial component of magnetic field inverses the polarity and the magnetic field lines in these zones are similar to an arcade shape. It is this arcade that supports the filament like figures 1.17 and 1.18 show.

Figure 1.16: Filaments observed on 1 May 2002 in $H\alpha$ radiation at the Paris observatory, filaments in black and the inversion line are the solid lines [8].

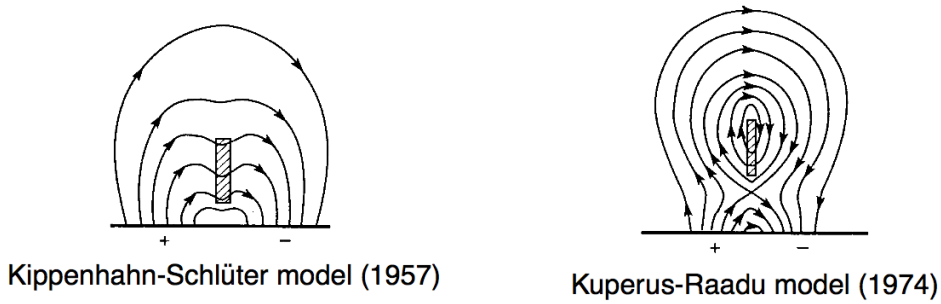

Figure 1.17: Two possible fields topologies. The solid lines are the magnetic field and the central rectangle represents the filament. The left panel represent the normal polarity (N-type) and the right panel represents the inverse polarity (I-Type).

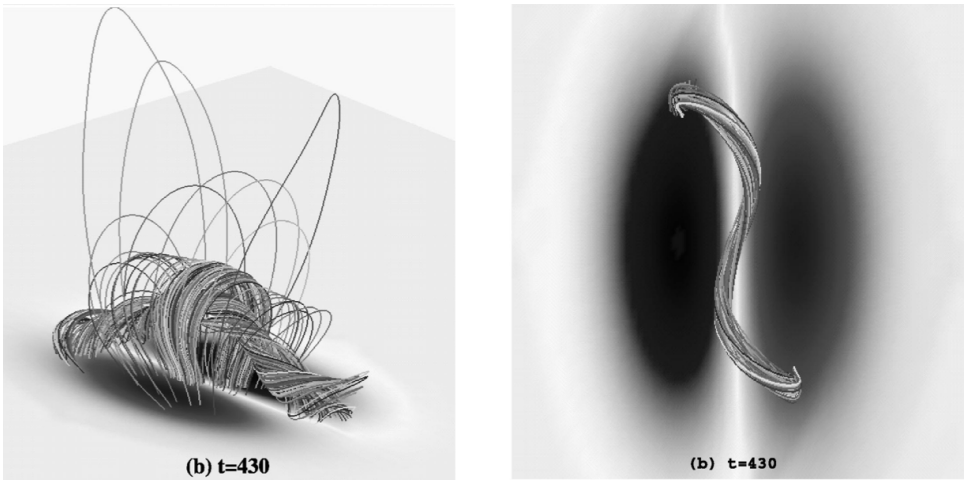

Figure 1.18: Simulation of a filament created by an active region where we see the coronal arcades and inside them the magnetic field lines belonging to the filaments [9].

But not all the neutral lines have the conditions to create and maintain filaments. The neutral lines where the filaments can appear are called the filaments channel [10], and represents the condition of maximum magnetic shear. In figure 1.19 we see a empty filament surrounded by active regions. In this image we see the orientation of magnetic field along the filaments which is determined by the polarity of the field in the ends of filament. Depending on the orientation of the magnetic field inside the filaments relatively to the field around we can define another property called chirality [9]. The chirality of filaments can be Dextral (dominates on north hemisphere) or Sinistral (dominates on south hemisphere). Figure 1.20 describes how it is defined.

The importance of chirality is that it can relate the magnetic field of the filaments with the magnetic field of the external environment.

Another behavior that is important to refer is the difference between filaments that have origin in the active regions and the filaments originated by the quiet sun [4].

The filaments originated by the quiet or quiescent sun are characterized by a life time of weeks or even of months, they can be very long and very stable.

The filaments originated by the active regions are characterized by life

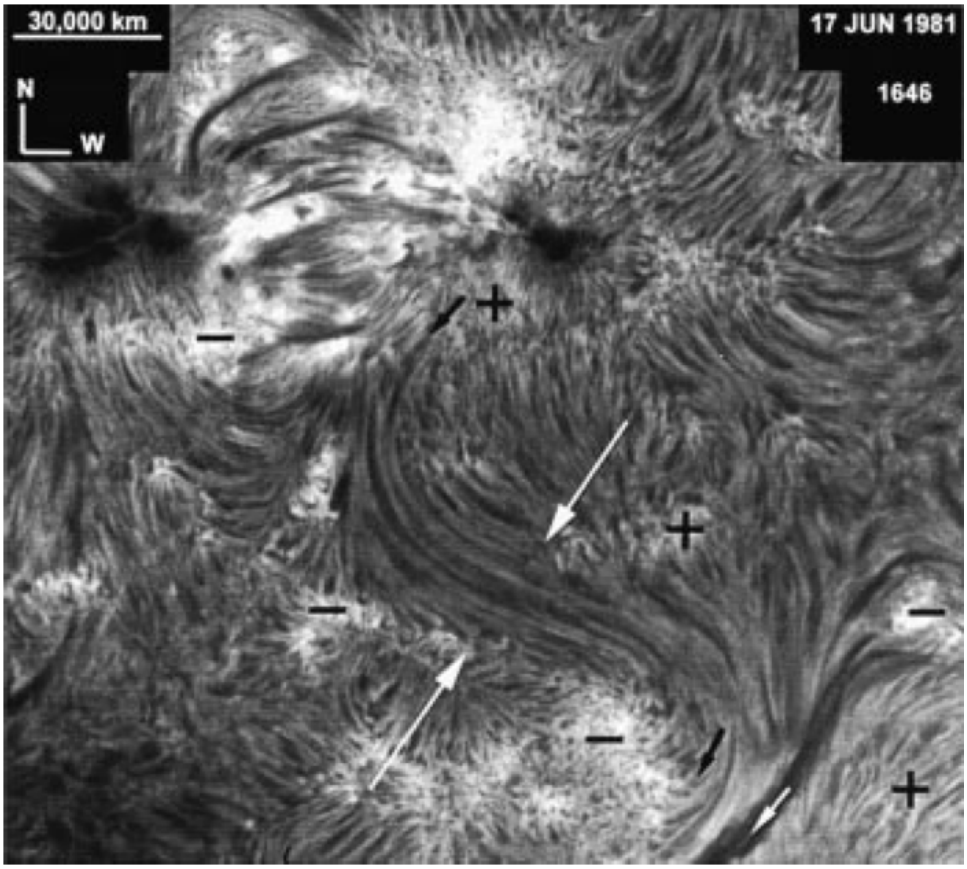

Figure 1.19: The zone between the long white arrows is the middle of an empty filament channel. This image was recorded at the Big Bear Solar Observatory.

Figure 1.20: Sketch of chirality definition.

time of hours or days and comparing to the quiescent filaments are much shorter. Because only the active regions appear at latitudes near the equator only in regions near the equator are this type of filaments observed.

Chapter 2

Statistic study of filaments behavior

I start in this chapter by describing the instrumentation and the program developed that provides the data used in the statistic studies.

The objective of these statistic studies is to obtain the parameters that I need to input in the simulation like the Carrington longitude and latitude of appearance of the filaments, the length and the limit where active filaments are observed. Note that in the Carrington coordinates system, lines of longitude rotate with the Sun. A prime meridian, analogous to the Greenwich meridian on Earth, was defined to coincide with the central meridian of the Sun, as seen from Earth, at a specific time on 9 November 1853 when R. C. Carrington began his observations. The rotation period of the coordinate system (prime meridian) varies throughout the year because of the changing distance of the Earth from the Sun, with an average value of 27.2753 days (the mean synodic period). A new Carrington rotation begins each time the prime meridian crosses the central meridian. The Carrington longitude of the central meridian is 360° at the beginning of the Carrington rotation, and decreases to zero at the end. The Carrington latitude (φ) is measured like latitude in the earth [11].

The statistical study that is made using the data in the HFC. All the data used in this chapter are bin extracted from the spectroheliograms obtained

during the cycle number 23 (start in May 1996 and end in Decembre 2008).

2.1 Data acquisition, and data handling.

2.1.1 Spectroheliograph

Since its invention separately by George Ellery Hale and Henri-Alexandre Deslandres in 1890, the spectroheliograph continues to be a good instrument for solar observation. The great advantage of using this instrument is the accuracy that we achieve in selecting the desired spectral lines.

In this section I will describe how the spectroheliograph of the University of Coimbra Observatory works [12]. Figure 2.1 is the scheme of such a spectroheliograph.

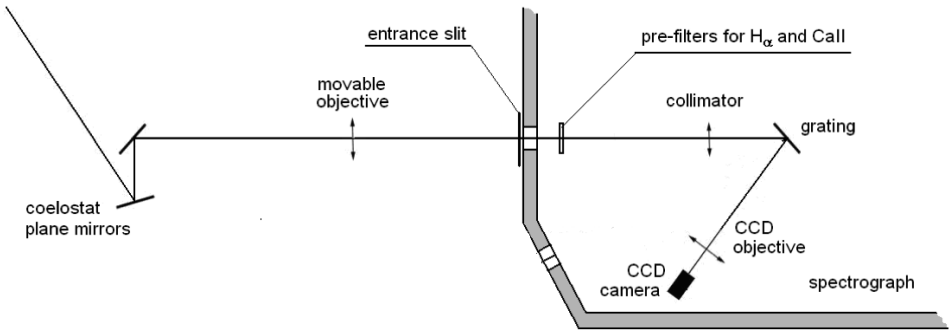

Figure 2.1: Scheme of the spectroheliograph of the University of Coimbra Observatory [12].

The first component is one coelostat. It consists in two mirrors placed in a motorized support that automatically track the movement of the sun. The coelostat is responsible for reflecting the light to the movable objective.

The movable objective is one convergent lens with focal length of 4060 mm and 250 mm of diameter. This lens is placed in one motorized horizontal plate and the movement of this plate is responsible for the shift of solar disc along the entrance slit. The solar disc diameter in the entrance slit has a maximum of 38.5 mm.

Light passes the entrance slit though one filter namely Hα and Ca II. Then, light goes trough the collimator, which directs it to one reflecting diffraction grating with 300 grooves per mm. It is this diffraction which grating allows us to choose the line of the spectrum that we pretend, Hα when using the Hα filter and K3 and K1 for the Ca II filter.

Finally, light enters in the CCD objective with an adjustable focal length between 200 - 240 mm which focuses the beam to the CCD camera.

The CCD camera and the associated software produce images in size with 1280×1024 pixels which can be written in the formats FITS, PNG and BMP.

2.1.2 Automatic detection

The large amount of data from the sun collected over the years implies that human processing of these data is an almost prohibitive task. To facilitate the processing of these data, many computer programs have been created. One of these programs aims at the automatic detection of filaments in the image developed in the Paris Observatory [13].

In an initial stage, the automatic detection code comprises several tasks namely correcting problems of sphericity of the sun, determining the center and radius of the solar limb [14].

The first task for standardization of the images is the limb fitting. Initially an approximation is made for the center and the radius of the disk. After this operation, a Canny edge detection (which is an algorithm for automatic detection of edges in images) is used to provide the candidate points for a fitting to an ellipse. Finally, the candidate points are fitted to an ellipse using least-squares approach.

When the determination of the elliptical geometry of solar limb is finished, the next task is the geometrical correction of the solar shape because during the data acquisition deformation on the solar shape is introduced. This geometrical correction consists of a translation of the centre of coordinates to the center of the ellipse, one rotation of the elliptical axis to make them parallel to the image edge, rescaling of the horizontal and vertical directions

to make the major and minor axes of sun the same size, 800 pixels. The matrix 2.1, represents this rotation plus the rescaling transformations,

$$\begin{pmatrix} a & b \\ d & c \end{pmatrix} = \begin{pmatrix} \frac{1}{S_x}cos^2\theta + \frac{1}{S_y}sin^2\theta & -\left(\frac{1}{S_y} - \frac{1}{S_x}\right)sin\theta cos\theta \\ -\left(\frac{1}{S_y} - \frac{1}{S_x}\right)sin\theta cos\theta & \frac{1}{S_x}sin^2\theta + \frac{1}{S_y}cos^2\theta \end{pmatrix} \tag{2.1}$$

where θ is the orientation of the principal axes of ellipse to the image axes and S_x and S_y are the ratios of the semi-major and semi-minor axes to the required radius.

The next correction operated in the image is the intensity normalisation. This operation corrects the limb darkening effect using one virtual image created by function 2.2,

$$I(\theta) = I(0)[1 - u_2 - v_2 + u_2cos(\theta) + v_2cos^2(\theta)] \text{ with } 0 \leq \theta \leq \frac{1}{2}\pi \tag{2.2}$$

where $I(0)$ is the intensity in the center of solar disk in the image, the parameters u_2, and v_2 have specific values for each image and can be determined by fitting the equation 2.2 to an meridian of the solar disk in the respective image [14], and θ represents the angle between the sun's radius and the line of sight through the centre of the disk counted from the center of the sun like figure 2.2 shows.

After these tasks are completed, an image enhancement is performed using a second derivate filter,

$$g(x, y) = f(x, y) - \nabla^2 f(x, y) \tag{2.3}$$

where,

$$\nabla^2 f = \frac{\delta^2 f}{\delta x^2} + \frac{\delta^2 f}{\delta y^2} \tag{2.4}$$

to facilitate the detection of the filament thinnest parts.

Now, to identify the filaments in the image a region growing procedure

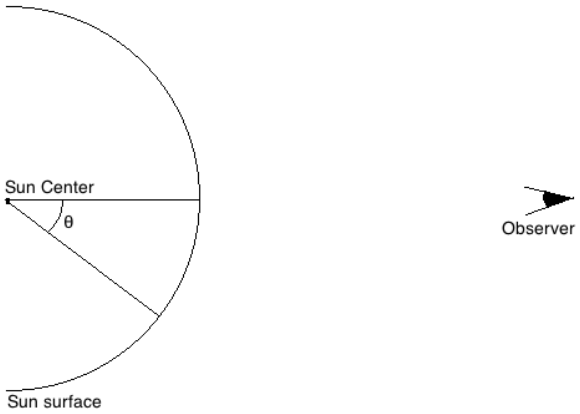

Figure 2.2: Scheme of the angle θ is measured.

is aplied. This procedure is based on the identification of seed that can be a single pixel or a group of contiguous pixels.

The automatic detection program to select a seed applies an threshold to the image. These thresholds are determined dividing the image into local square windows. In the case of the Meudon images the windows have the size of 1/6 of the original image. The threshold for each window is determined by,

$$T_{win} = QS_{win} - \alpha \times \sigma_{win} \tag{2.5}$$

where QS_{win} is the local quiet sun intensity, α is a constant (for Meudon image is set to 3.7) and σ_{win} is the standard deviation of the windows pixels.

After the seeds are determined, a bounding rectangle is defined from the location and size of the seed. The growing process is applied for each rectangle using the following limits of the intensity,

$$T_{upp} = QS_{br} - \beta \times \sigma_{br} (\beta < \alpha) \tag{2.6}$$

$$T_{low} = 0 \tag{2.7}$$

where QS_{br} is the rectangle intensity, β is constant (for Meudon image is set to 1.5) and σ_{br} is the standard deviation of the rectangle pixels.Figure 2.3 shows the process of filaments detection.

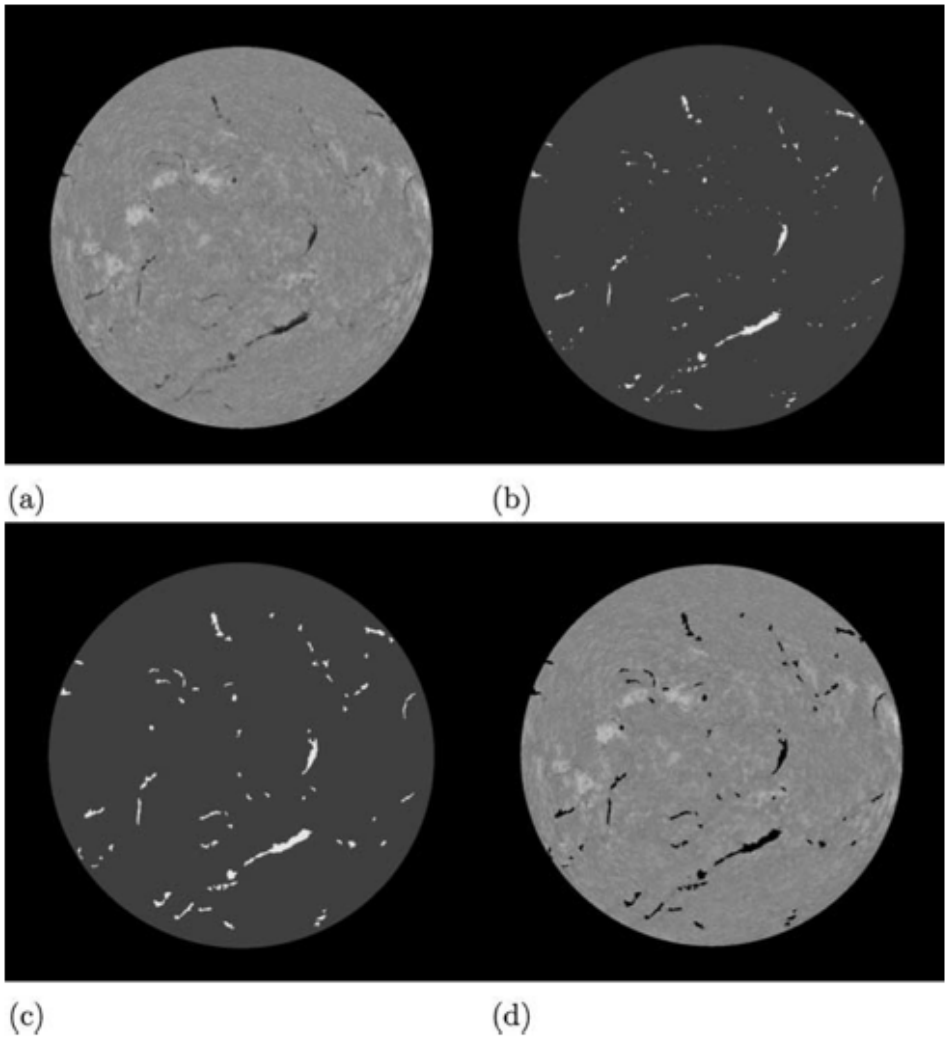

Figure 2.3: Segmentation results for the 1st of April 2001, 08:45:00 UT: (a) original Hα image from Meudon, (b) seeds detected, (c) region growing results and (d) original and results superimposed [13].

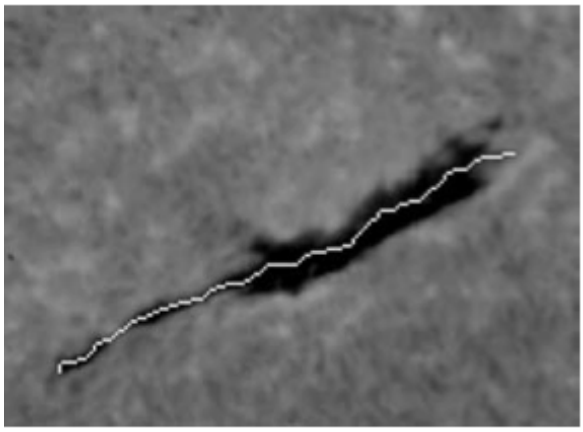

Figure 2.4: Filament skeleton (white line) superimposed on the original image [13].

Finally, a succession of convolution processes identify the structure and extract its skeleton. The solar filament is reduced to a single line of the filament as figure 2.4 shows.

2.1.3 HFC database

The HFC database, stores all data extracted from the observation inside the HELIO [15] project. The data in HFC are distributed over several tables. The names of these tables are shown in table 2.1.

Table 2.1: Tables in the HFC

OBSERVATORY
OBSERVATIONS
PP_OUTPUT
FRC_INFO
CORONALHOLES
CHGROUPS
VIEW_CH_FULL
ACTIVEREGIONS
VIEW_AR_FULL
FILAMENTS
FILAMENTS_TRACKING
VIEW_FILAMENTS_FULL

The OBSERVATORY table contains information about observatory, telescope and instruments where the observations were made. The OBSERVATIONS table contains information about the original image. PP_OUTPUT contains information about the pre-processing code and cleaning code. FRC_ INFO contains information about version of code and its operator. CORONALHOLES, CHGROUPS and VIEW_CH_FULL are tables containing information about coronal holes. ACTIVEREGIONS and VIEW_AR_FULL are tables containing information about active regions. FILAMENTS and VIEW_ FILAMENTS_FULL contain information about filaments and FILAMENTS_ TRACKING contains information extracted from the filament tracking code. For this study I mainly use the last table of the HFC, which is described in more detail in table 2.2.

Table 2.2: Description of the VIEW_FILAMENTS_FULL table. The information inside this table is extracted from the automatic detection program [13].

FIELD	**COMMENT**
DATE_OBS	Date and time of the start of the observation in UTC
DATE_END	Date and time of the end of the observation in UTC
C_ROTATION	Carrington rotation
CDELT1	Spatial scale of the original observation (X axis) (in arcsec)
CDELT2	Spatial scale of the original observation (Y axis) (in arcsec)
BITPIX	Coding of the pre processed image
NAXIS1	First dimension of the image used for detection (X)
NAXIS2	First dimension of the image used for detection (Y)
CENTER_X	X coordinate of sun centre in pixels
CENTER_T	Y coordinate of sun centre in pixels
R_sun	Radius of the sun in pixels
ID_FIL	Index to identify file and link files together
FRC_INFO_ID	Ref. to FR code information
PROCD_OBS_ID	Ref. to processed observation where detection was made
RUN_DATE	Date when FR code was run
C_ROTATION	Carrington rotation
SC_ARC_X	X coordinate of skeleton centre in arcsec
SC_ARC_Y	Y coordinate of the skeleton centre in arsec
SC_CAR_LAT	Carrington latitude of skeleton centre (degrees)
SC_CAR_LON	Carrington longitude of skeleton centre (degrees)
FEAT_NPIX	Number of pixels included in the feature
FEAT_AREA	Area of the feature in square degrees
FEAT_MEAN2Qsun	Mean of the feature to QS instensity ratio
BR_ARC	Bounding rectangle coordinates in arsec
BR_PIX	Bounding rectangle coordinates in pixels
FEAT_MAX_INT	Feature max. value, in units of the original observation
FEAT_MIN_INT	Feature min. value, in units of the original observation
FEAT_MEAN_INT	Feature mean intensity value in the units of the original obs.
CC_PIX_X	X coordinate of chain code start position in pixels
CC_PIX_Y	Y coordinate of chain code start position in pixels
CC_ARC_X	X coordinate of chain code start position in arcsec
CC_ARC_Y	Y coordinate of chain code start position in arcsec
SKE_LEN_DEG	Length of the filament in degrees
CURVATURE	Index of curvature of the skeleton
ELONG	Elongation factor
ORIENTATION	Orientation of the filament
COD_SKE_PIX_X	X coordinate of skeleton chain code start in pixels
COD_SKE_PIX_Y	Y coordinate of skeleton chain code start in pixels
COD_SKE_ARC_X	X coordinate of skeleton chain code start in arcsec
COD_SKE_ARC_Y	Y coordinate of skeleton chain code start in arcsec
CHAIN_CODE	Boundary chain code
CHAIN_CODE_SKE	Skeleton chain code
ID_ASCII	
CCODE_LNTH	Chain code length
CCODE_SKE_LNTH	Skeleton chain code length
PR_LOCFNAME	Name of the corresponding pre_processed image file

2.2 Carrington longitude preferential zones

The main goal of this section is to test the possibility that there exist preferential zones of Carrington longitude where filaments are observed.

We start making the histogram of the Carrington longitudes of filaments skeleton center for all filaments observed in a period of 5 days (for example from the day 01-01-2000 to the day 05-01-2000) and plot these as shown in figure 2.5. Then, we make a shift of one day (02-01-2000 to 06-01-2000) and

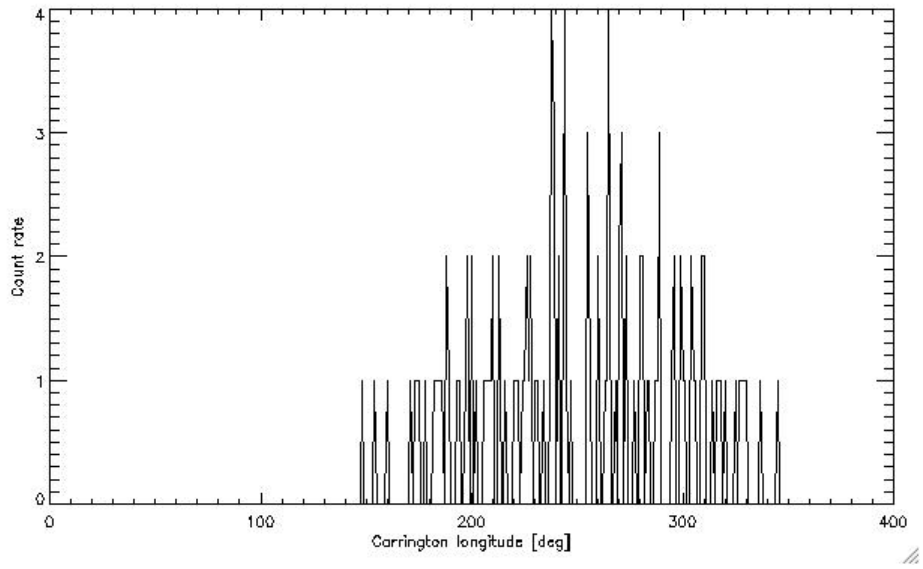

Figure 2.5: Histogram with bin size of 1 of Carrington longitude for 5 days.

make the plot again. This process is applied for all 11 years cycle, starting in 01-01-1997 and finishing in 12-29-2008. In the end, I made a movie with all histograms in order to try to observe the existence of preferential zones in longitude.

The analysis of the film and also the individual images like figure 2.5 shows the existence of a distribution around a single maximum for each image. We also see the shift of the centre of this distribution when we look for the sequential images.

One first reason to explain this behavior is the variable efficiency of program detection which is better for the image center and worse close to the

limb. The center of the distribution is then the Carrington longitude of the center of images and the tails of the distribution are the Carrington longitudes of the observable solar disk extremes where the efficiency of the program is poorer. During these 5 days we look more often for a central Carrington longitude of the distribution than for the more extreme Carrington longitudes.

A second reason to explain the observed behavior is because when looking the sun during five days interval we don't see all the sun surface but only a portion in the Carrington longitude map and this portion changes after the shift of one day. So the combination of variable of detection efficiency and the fact that we can only see a portion of the sun in each histogram produce the global distribution showed in figure 2.5 and the apparent movement of this distribution.

I can consider that the filaments don't have Carrington longitude preferential zones where they can be observed, based on the description of the described phenomena.

This behavior is expected because all solar mechanics and MHD effects that influence the filaments operate (on a global point o view) independently of longitude. This conclusion is taken into account in the simulation, where the filaments are created uniformly in longitude.

2.3 Carrington latitude of filament skeleton center

2.3.1 Observation

The aim of this section is to verify the existence of preferential zones in Carrington latitude for the observation of the filaments skeleton middle point or center.

We started to determine the histogram of the Carrington latitude of filaments ϕ skeleton center, using the data for the whole solar cycle and obtained the histogram showed in figure 2.6.

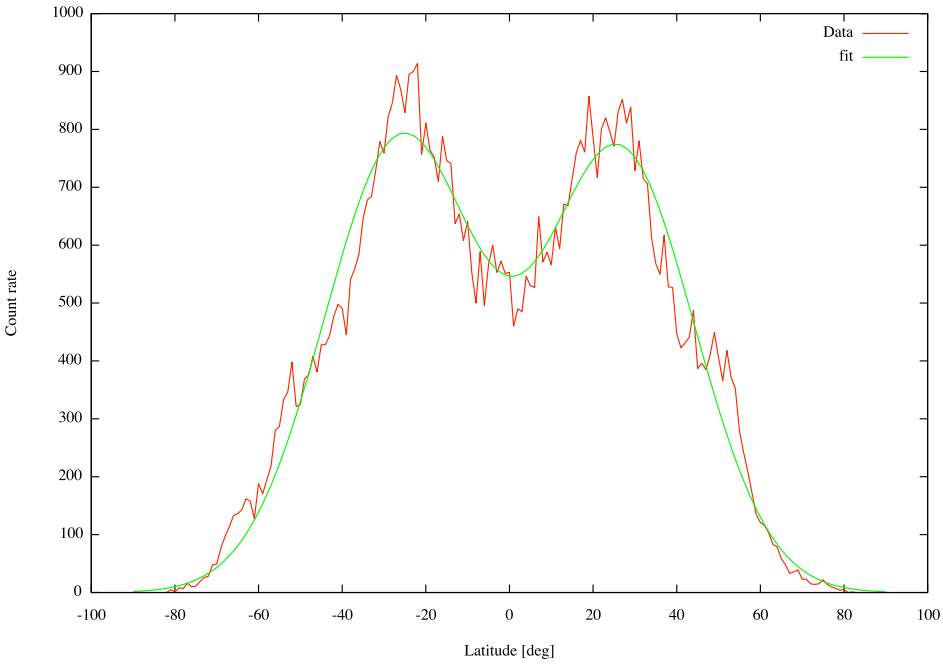

Figure 2.6: Histogram with bin size of 1 of the Carrington latitudes of the observed filaments and best fitted curve with two gaussianans.

From the analysis of the histogram, we see that a two gaussians curve, given by, equation 2.8, can be fitted to it.

$$f(\varphi) = a \exp\left(\frac{-(\varphi - \mu_1)^2}{b}\right) + c \exp\left(\frac{-(\varphi - \mu_2)^2}{d}\right) \tag{2.8}$$

Table 2.3 shows the parameters obtained.

Table 2.3: Values obtained for the parameters of equation 2.8 by fitting two gaussians to the data showed in figure 2.6. The corresponding curve is showed in the same plot.

	Values
a	8394.6 ± 151.5
μ_1	-25.8 $\pm$ 0.5
b	18.3 ± 0.5
c	8064.7 ± 154.1
μ_2	26.3 ± 0.5
d	17.9 ± 0.5

From the histogram of the latitudes of the filaments we saw two distinct peaks with mean latitudes of -25.8 and 26.3. These distributions have origin in the existence of active regions which promote the formation of filaments. We also verified that the parameters related to the sigma of the gaussians (b and d) are the same for both gaussians, tacking into account the errors of the fit. This indicates that the phenomena that create the distribution of the filaments in latitude are equatorially symmetric.

The height of the gaussians show a small difference between the two hemispheres. This is expected, because an asymmetry in the solar activity between the two hemispheres is observed [16] and the north hemisphere was more active than the south during the considered period of study.

2.3.2 Drift

In this subsection we study the evolution of Carrington latitude of filaments skeleton center in order to extract a possible drift velocity for filaments appearance. I begin to make an histogram of Carrington latitudes of the filaments skeleton centre for only one Carrington rotation. After that, I fit two gaussians to the histogram of the Carrington latitudes and save the value of the mean of the gaussians in a table. This process is repeated for the whole cycle, starting in the Carrington rotation number 1909 and finishing in the rotation number 2085. In the end, I plot all mean values of the gaussians

that I have obtained for each Carrington rotation and make a linear fit, because we are only interested in the global drift, for the whole series of data. The plot of the mean values of the gaussians and the linear fit are showed in figure 2.7.

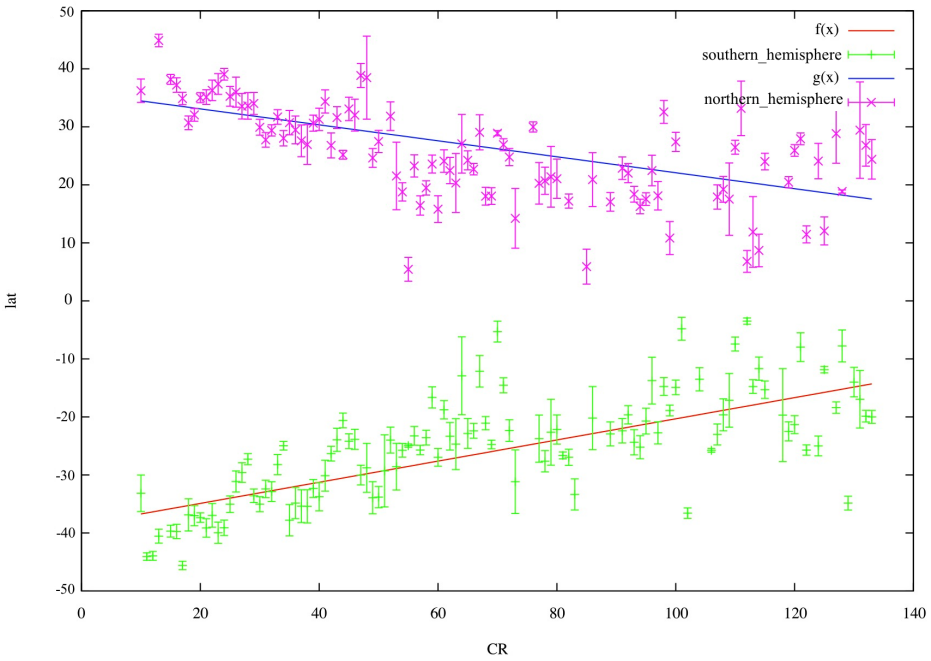

Figure 2.7: Plot of the mean values of the gaussian for each hemisphere and the respective linear fit.

Note that not all data obtained for mean values are shown in the figure 2.7, because sometimes the error on the fit of the gaussians is very high ($> 10^{o}$). This was to be expected, because during the solar minimum or in periods of low solar activity the number of filaments is very low and the number of points to make the fit is not enough. Table 2.4 shows the slope obtained for the fitted straight line.

We will now concentrate on the ascending phase of solar cycle that goes up to Carrington rotation number 1958. During this the distribution is different and we can extract more information using another fitting curve. This new curve is given by equation 2.9, representing a linear curve coupled to an harmonic oscillation with variable amplitude linearly changing with latitude,

Table 2.4: Slopes obtained by the linear fitting the data for Carrington latitude of filaments for each Carrington rotation during all cycle. The slope is in deg/CR.

	f	g
Slope	0.182 ± 0.018	-0.137 ± 0.023

and was chosen only because they fit relatively well the data.:

$$f(\mathrm{CR}) = m_l \mathrm{CR} + b_l + c_l \mathrm{CR} \sin(\omega_l \mathrm{CR}) \tag{2.9}$$

The values obtained for the parameters in equation 2.9 when fitting it to the data, for each series of data (northern and southern hemisphere) are showed in table 2.5. The data used and the curves obtained after the fitting are represented in figure 2.8.

Table 2.5: Values obtained for the parameters of equation 2.9 when fitting the data showed in figure 2.8. The fitted curves are shown in the same plot.

	Blue (southern)	Purple (northern)
m_l	0.43 ± 0.04	-0.27 ± 0.04
b_l	-43.3 ± 0.70	38.02 ± 0.95
c_l	0.17 ± 0.03	-0.13 ± 0.03
ω_l	0.412 ± 0.005	0.313 ± 0.007

From this study we saw a drift of the filaments location distribution from regions more distant from the equator to regions closer to the equator. For the northern hemisphere filaments, the rate of drift is $0.182 \pm 0.018 deg/CR$ and for southern filaments the rate is $0.137 \pm 0.023 deg/CR$ like table 2.4. This drift can be understood if we look for the distribution of the active regions. The active regions start to appear more frequently at high latitudes and drift for lower latitudes with the evolution of the cycle. So, the existence of the distribution of the filaments appearance drift results from the appearance drift of the active regions.

When only the ascending phase of the solar cycle is considered we saw the same global drift of the filaments skeleton centre from higher latitudes to latitudes more close to the equator, as figure 2.7 shows. Concerning the

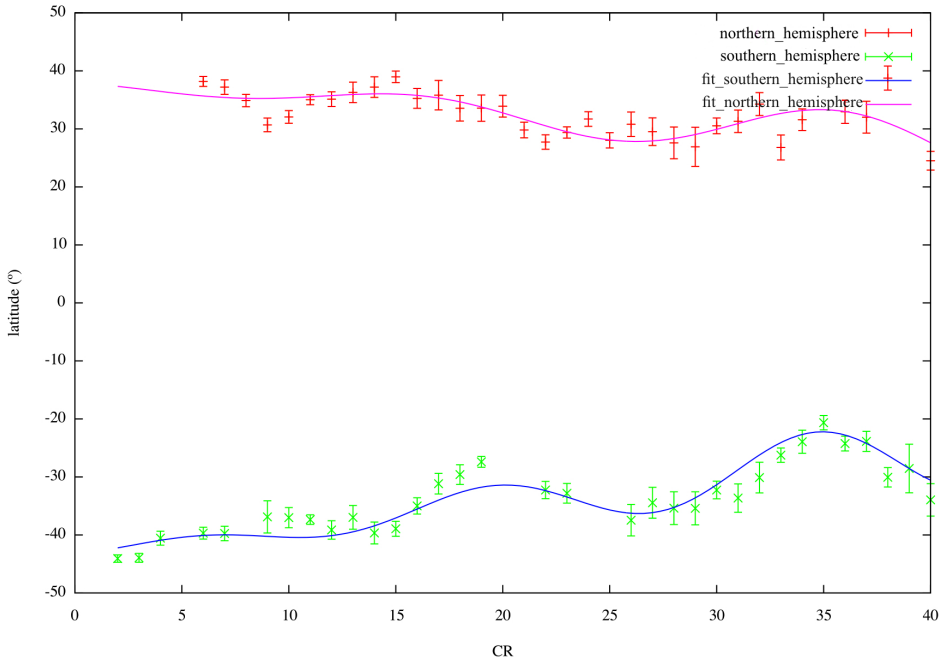

Figure 2.8: Data obtained for the mean of the various gaussian fitting for the latitude for each Carrington rotation. In this plot are also shown the fitted curves given by equation 2.9.

oscillation behavior, we see in both hemispheres approximately the same rate of increase of the amplitude but a small difference in the oscillation period. I don't find any plausible explanation for this behavior.

2.4 Length of the filament

We describe the study of the length of the filaments skeleton, where the length of the filament is the length of filament skeleton and is measured in degrees like figure 2.2 shows.

The idea is to see if the length of the filaments skeleton follow some distribution.To try to understand this behavior we made the histogram of the length of the filaments skeleton for the whole solar cycle. The result is shown in figure 2.9, where we saw that filaments with lengths between 1.5 and 2.5 deg are the most frequent. Between 0 and 1.5 deg the distribution

looks linear and for lengths greater then 2.5 deg the distribution appears to follow an exponential decay. The high number of filaments with small length comes from the contribution of both quiescent filaments and filaments from active regions, so the population is so high. The filaments of high lengths came only from quiescent filaments and the population is smaller.

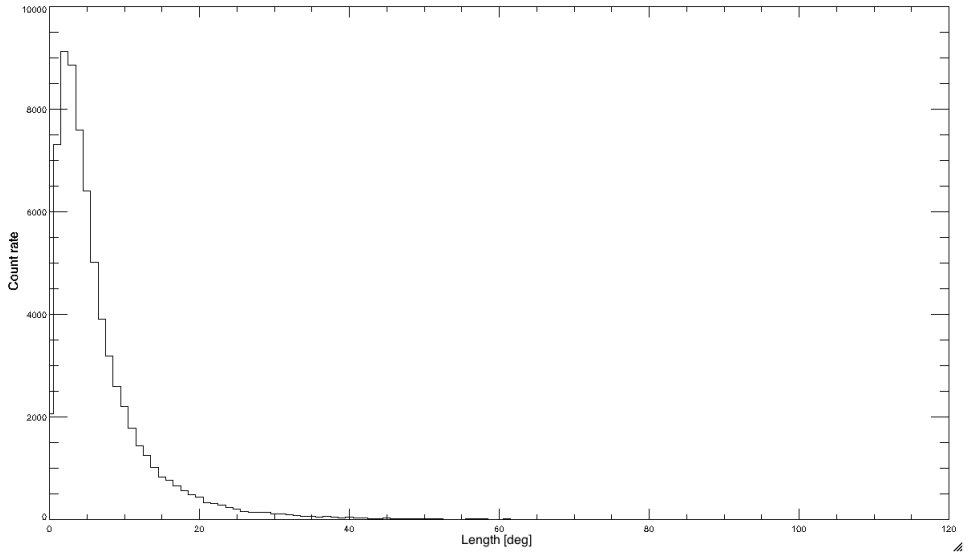

Figure 2.9: Histogram with bin size of 1 of the length of the filaments skeleton.

2.5 Curvature

In this section we will explain the analysis we made concerning the curvature of the filaments. The curvature is described using the curvature index, defined as,

$$\text{ci} = 10(1 - \frac{d}{l}) \tag{2.10}$$

where d is the distance between end points of the filament skeleton and l is the length of the filament.

I start to do the histogram of the curvature index for the whole cycle as figure 2.10 shows.

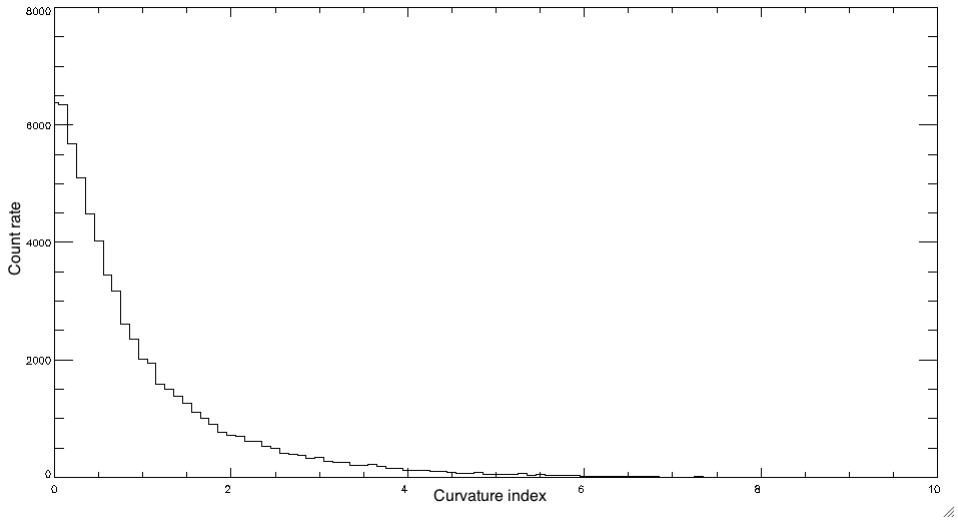

Figure 2.10: Histogram with bin size of 0.1 of the curvature index of filaments along the whole cycle.

We observe that the the distribution looks like to follow one exponential distribution of probability.

To test this behavior and check if the parameters of this distribution change along the cycle, I made the same histogram but for each Carrington rotation and fitted the data to an exponential decay distribution, given by equation 2.11. The plot of the decay factor (b) obtained for each Carrington rotation is shown in figure 2.11.

$$f(\mathrm{ci}) = a_{c1} e^{-b_{c1}\mathrm{ci}} \tag{2.11}$$

From this analysis we observe that the decay factor apparently follows a sinusoidal curve. By fitting with equation 2.12 we obtain the values in table 2.6.

$$f(\mathrm{CR}) = a_{c2} \sin(\omega_{c2}\mathrm{CR}) + c_{c2} + d_{c2}\mathrm{CR} \tag{2.12}$$

Table 2.6: Values obtained for the parameters of equation 2.12 by fitting it to the data showed in figure 2.11. The corresponding curve is shown in the same plot.

	f(CR)
a_{c2}	0.031 ± 0.003
ω_{c2}	0.0393 ± 0.0009
c_{c2}	0.095 ± 0.005
d_{c2}	$0.0001 \pm 6 \times 10^{-5}$

From the study of curvature of filaments, we see that the distribution of the curvature index is similar to an exponential decay. The existence of a greater number of filaments with low indices of curvature can be understood by the existence of a greater number of filaments with low length, that are more hard to curve. The existence of filaments with very high curvature index is rare, because it requires more energy. In the second part of the study of the curvature index we saw that data represented in figure 2.11 is well described by a sinusoidal behavior. This behavior can be interpreted by the fact that in the beginning of the cycle the filaments are less curved, because the magnetic energy is not so high at the surface and the magnetic field is not so turbulent. With the evolution of the solar cycle, the magnetic field increases on the surface and it's more frequent the appearance of more curved filaments. We also see that the drift component is not significant.

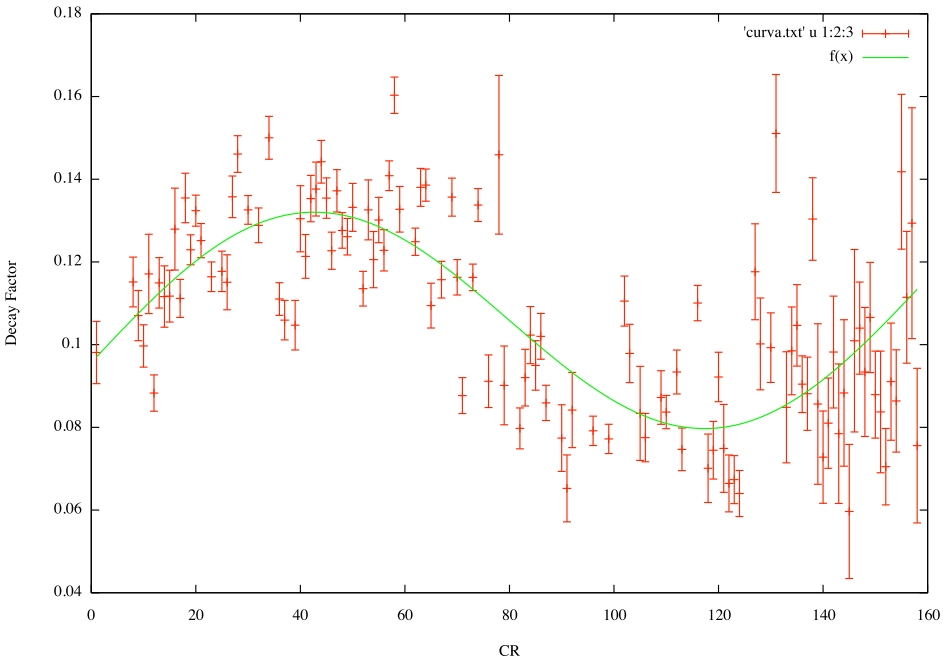

Figure 2.11: Data for the decay factor, obtained from the fitting of equation 2.11 to the curvature for each Carrington rotation. In this plot is also shown the curve fitted to the data using equation 2.12.

2.6 Correlation between active regions and filaments.

In this section, the idea is to verify if we can divide the sun in regions where active regions interfere with the filaments appearance. The two zones that I expect is one where active regions are not observed (low latitudes) and another where active regions are observed (high latitudes).

To see this I plot the histogram of latitudes of the filaments and active regions in a interval of time of one year. Figure 2.12 shows one of the histograms obtained for the Carrington latitude of active regions.

Here we see that active regions are located between 50 and -50 degrees of latitude, with a maximum at $\approx \pm 20^{o}$, and much less active regions can be found close to the equator, during all cycle like figure 1.8 shows. From this I can consider that the existence of active regions can only interfere with filaments between 50 and -50 degrees of latitude where we observe much more filaments except in the latitudinal belt close to the equator where we have much less active regions and in latitude higher than $|50^{o}|$.This study has been done previously by [17].

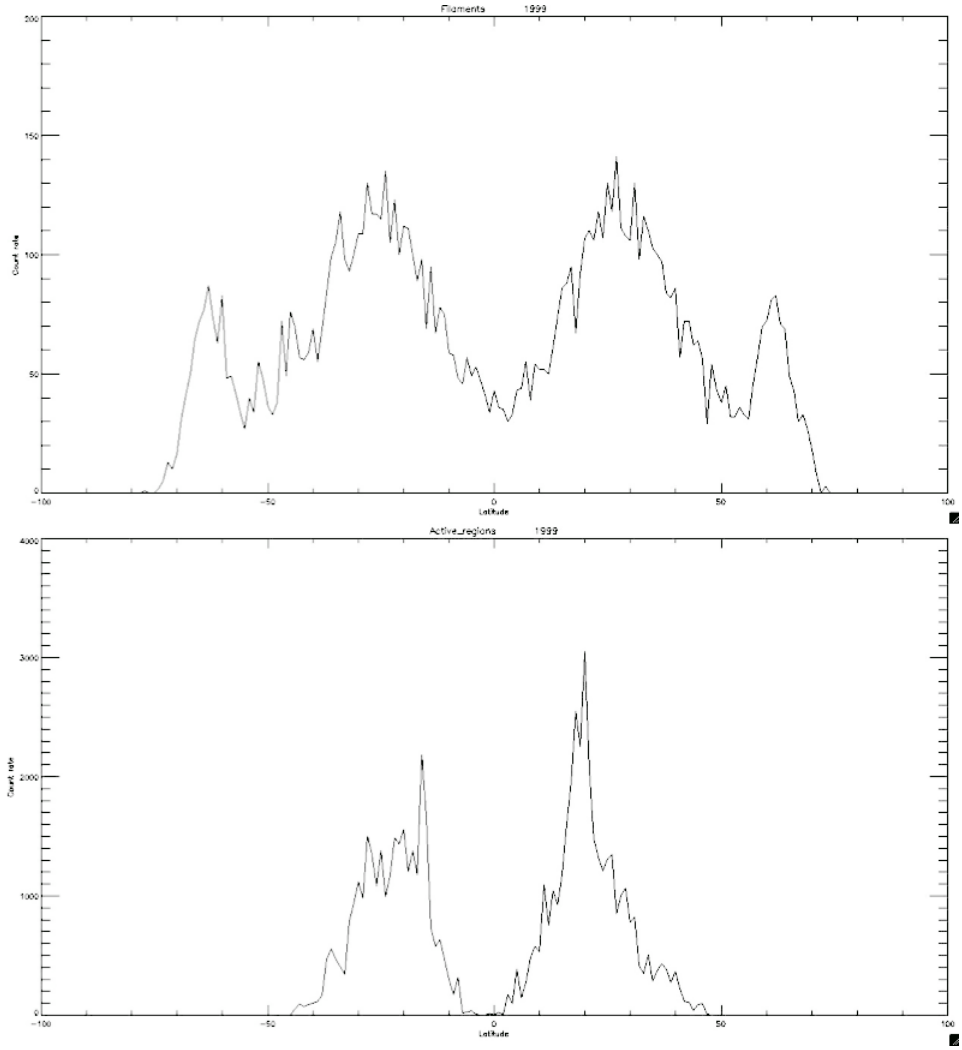

Figure 2.12: The top panel is the histogram with bin size of 1 of the latitude of the filaments skeleton center in the year 1999. The down panel is the same histogram but for the active regions center.

2.7 Orientation of filaments

This section describes the study of the orientation of filaments. In particular how perspective can change significantly the orientation observed.

The orientation is measured using a linear fit to the filament to obtain the angle between the filament and the equator of the image. Figure 2.13 shows how the angle is measured.

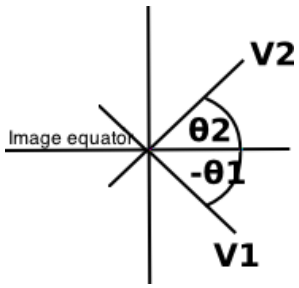

Figure 2.13: Scheme showing how the orientation angle is measured relative to the equator line.

To see if the region where the filaments are observed or the perspective effect changes the distribution of the observed orientation we divide the sun disk in quadrants. For each quadrant we made the histogram of the orientation and obtained the plots showed in figure 2.15.

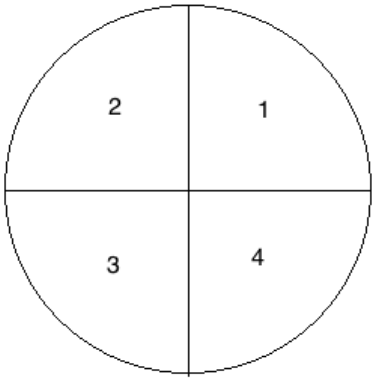

Figure 2.14: Number attributed to each quadrant.

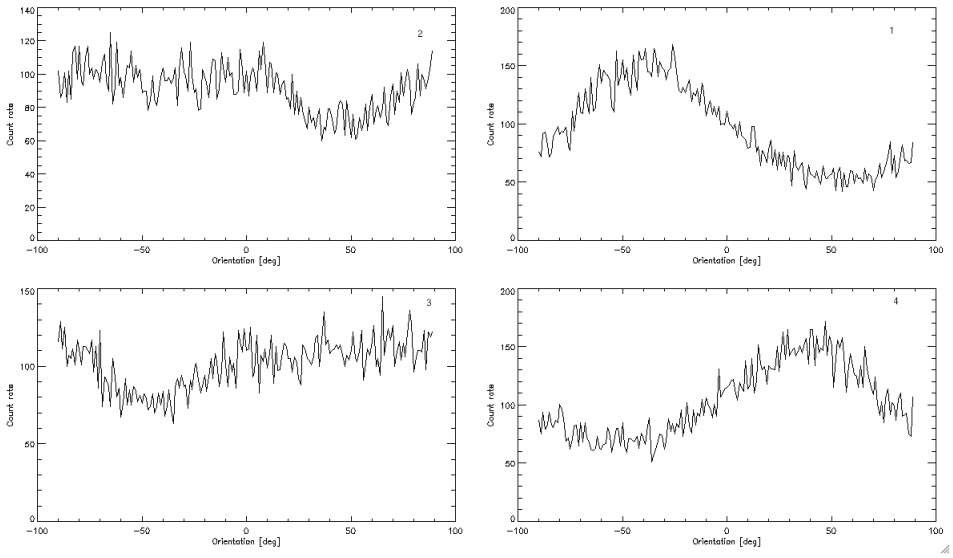

Figure 2.15: Histogram with bin size of 1 of orientation of filaments per quadrant. Top right panel correspond to the first quadrant. Top left panel correspond to the second quadrant. Down left panel for the third quadrant. Down right panel for the fourth quadrant.

In Figure 2.15 we see that the distribution of filaments orientation seems to depend on the quadrant where it is observed.

After seeing that it is in fact possible that the perspective can change the orientation distribution we divide the sun again. This is because in the previous division we include zones of the sun where the perspective effect is small (center of the disk) and zones where the perspective can be much more important (close to the limb).

The second division consist in separating each quadrant in 4 parts like shown in figure 2.16. To each part we call "octant".

For each "octant" we calculate the histogram of the orientation angle and obtain the plots shown in figure 2.17.

From the analysis of figure 2.17 we expect that the "octants" numbers, 2-3-5-8-9-12-14-15, don't show any relevant perspective effect, even if we can see a small difference between then, because these "octants" are close to the central meridian of sun disk, where the perspective effect is smaller. Assuming this approximation, when we look to the right "octants" we observe a

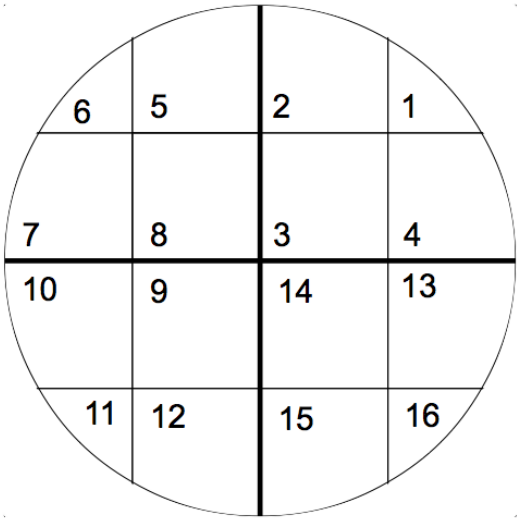

Figure 2.16: Number attributed to each "octant".

symmetric shift of the maximum peak for greater inclinations. This behavior is not observed in the left "octants" where for "octants" 6 and 11 we observe a uniform distribution and for "octants" 7 and 10 we observe that the filaments are preferentially observed with high inclinations.

The differences between the right and left "octants" are difficult to understand because I would expect the perspective effect to be symmetrical between both north and south hemispheres,which is observed, and between left and right sides of the sun disk, which is not observed.

Another element that can produce an effect in observed orientation is the solar rotation, that create a outward velocity in the left "octants" and inward velocity in right "octants". But for the filaments the solar rotation is equal independently of where it is observed. Due to this if the rotation changes the orientation of the filaments this has a different effect on different octants because it is observed at different points resulting in an effect of perspective.

It was to try to solve this question that the simulation was created.

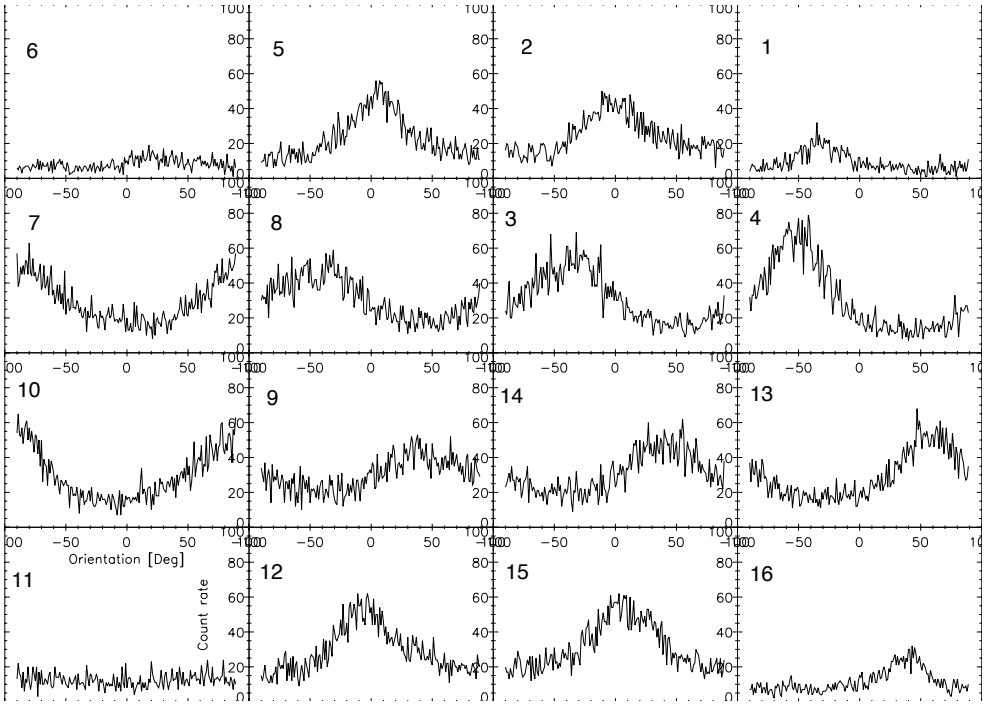

Figure 2.17: Histogram with bin size of 1 of the orientation of filaments per "octant".

Chapter 3

Simulation

In this chapter I will describe the model and its implementation, using IDL language, that was developed during this thesis to simulate the observation of the filaments orientation and to understand what the effects cause the peculiar behavior in the observed orientation.

The main idea of this simulation is the random creation of filaments in the solar surface, using Monte Carlo techniques, projecting them in a plane like a photograph plate and calculate the orientation of each filament to try to obtain the same distribuction as in figure 2.17.

To achieve this, I start to determine the initial parameters to create the filament:

- Longitude appearance of filaments skeleton center
- Latitude appearance of filaments skeleton center
- Length of filament skeleton
- Initial Orientation

Based on the study described in section 2.2, the longitude of appearance of the filaments skeleton center is distributed uniformly in the interval of 0 to 2π.

To determine the value of the latitude appearance of filaments skeleton center, we use the study explained in section 2.3.1, with determination of the

probability distribution $f(\varphi)$. Related to the length of the filaments we use the study described in section 2.4 to determine its probability distribution function.

Then, we calculate the NCDF for the latitude and the length of the filaments, obtained by:

$$F(x) = \frac{\int_a^x f(x)dx}{max(\int_a^b f(x)dx)} \tag{3.1}$$

The NCDF obtained for the latitude appearance of filaments skeleton centre, is shown in figure 3.1, and the NCDF for the length of filaments skeleton,is shown in figure 3.2.

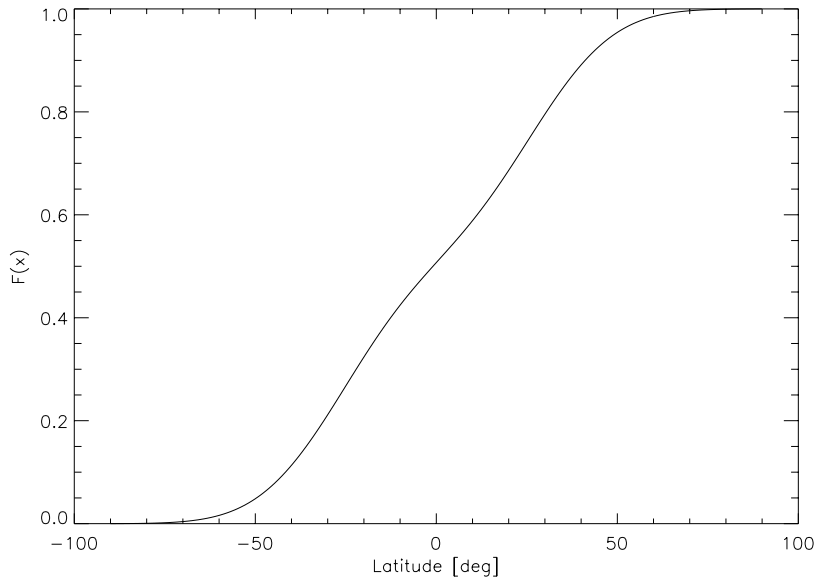

Figure 3.1: NCDF obtained for the latitude appearance of filaments skeleton centre.

The next step is the characterization of the initial orientation at which the filaments appear. To our knowledge such distribution was not published yet. For this reason, to find an initial orientation distribution is a crucial point of this work. To create this distribution, we first divide de sun in two

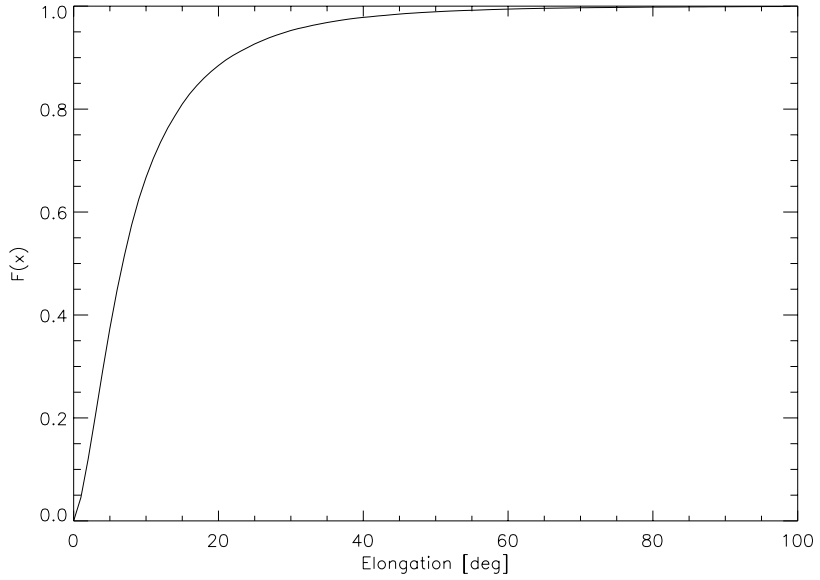

Figure 3.2: NCDF obtained for the length of filaments skeleton.

different regions based on the study described in section 2.6. The first zone considered is the active zone, where the influence of the presence of active regions dominates, it extends from latitudes -50 to 50 degrees. The other zone is the quiescent zone, where the phenomena of a quiet sun dominate, it extends from latitudes higher than 50 and lower then -50 degrees.

Based on the characteristics of each zone I consider a simple model assuming that:

- Do to the relation between the active regions and filaments, in the active zone the filaments appear preferentially inclined and in the quiescent zone we consider that the filaments appear parallel to the equator.

- On the frontier between the two zones the value of orientation in the maximum of each distribution must be equal due to continuity of the physical environment.

- Close to the equator the filaments have the preferential orientation of 0 degrees.

- A component is present, representing an isotropic orientation for the appearance of solar filaments.

Equations 3.2 and 3.3 are the distribution functions used in the active zone and in the quiescent zone, respectively.

$$f(O,\varphi) = a_1 + b_1 \times \exp\left[-\frac{(O + d_1 \times \sin(3.6 \times \varphi - 5.65))^2}{c_1}\right] \tag{3.2}$$

$$f(O) = a_2 + b_2 \times \exp\left[-\frac{O^2}{c_2}\right] \tag{3.3}$$

Where O is the orientation of the filaments (denoted by θ in fig. 2.13), φ is the Carrington latitude, a_1 and a_2 are the parameters that represent an isotropic component of orientation distribution, b_1 and b_2 are the amplitude of the gaussiana, c_1 and c_2 are related to the variance of the gaussian and d_1 is the amplitude of *sinus* function. The value 3.6 $rad\ rad^{-1}$ (spacial angular frequency) and the value -5.65 rad (phase) in equation 3.2 are calculated to satisfy second and third conditions. Both equations express a gaussian distribution for each latitude, but the equation 3.2 there is a *sinus* curve dependent on latitude that moves the center of the gaussian, as a result of the interaction between filaments and active regions.

Now, I have to create the filaments skeleton over the solar disk. For this task, I introduce the height and shape of the filaments skeleton over the solar surface. First a *sinus* curve was used to describe the shape of filaments for the height of this *sinus* curve we used the height of the chromosphere and tested the hypothesis that the height change with the length of filaments. These two implementations have not worked since we verified that they cannot reproduce filaments with strong inclinations, like figure 3.3 shows.

Then I approximated the shape of filaments to a line that follows the solar curvature considered as the altitude of the chromosphere, and verified that the result is much better with this approximation.

This approximation can be based on the fact that, as I said in the introduction the filament is a vertical structure above the photosphere and what

we see in the spectrographs is the top of this structure inside the chromosphere, looking like a linear structure in the solar disk.

The evolution of the filaments is determined by two elements: the differential angular velocity and the life time of the filaments. The differential angular velocity model used in this simulation is the same as for the photosphere and is given by [18]:

$$\omega_S = A + Bsin^2\varphi + Csin^4\varphi \tag{3.4}$$

where parameters A, B and C can be measured using different techniques. In this study, I used the values obtained by Snodgrass and Ulrich in 1990 using the differential rotation of supergranules from MWO daily dopplergrams. The value for each parameter are $A = 2.972\ \mu\ rad\ s^{-1}$, $B = -0.484\ \mu\ rad\ s^{-1}$ and $C = -0.361\ \mu\ rads^{-1}$.

Concerning the lifetimes of filaments in this simulation I don't use any type of distribution to describe them. Instead, I fix a value for the lifetime of filaments of 10 days. The main problem of this approximation is related to the difference between the lifetimes of active filaments, less durable but more numerous, and quiescent filaments, more durable but less numerous. This value that I give to the lifetimes of filaments tries to describe both types of filaments.

At this point I have all parameters necessary to create filaments randomly and make evolve the filaments based on the assumptions and approximations considered. The period of the random number generator is $2^{32} - 1$ [19].

First, I verify if the filament appears in the observable side of the sun. If it stays in the observable side of sun, the program calculates its projection on a plane representing a photographic plate, in this case the XZ plane is considered. Using this projection, the center of the filament skeleton and the orientation of the filament are calculated. The center of the filament skeleton is defined by the central point of the projected filament. The orientation is obtained by a linear fit to the projected filament and using the slope of the fit I calculate the angle between the filament and the image equator, as was described in section 2.7. These two values are saved for future treatment.

The next step is to calculate the position of the filament after one day, because this is the mean frequency with which the spectroheligrams are made, and again to calculate the center of the filament skeleton and the filaments orientation to save them for future treatment. This operation is repeated 10 times, which is the assumed lifetime. Note that if the filament is created in the non observable side of the sun, it is not recorded during the time it stays there. But when in its evolution it goes to the visible side, its starts to be recorded. The inverse happens when the filament appears in the visible side of the sun and during its evolution goes to the other side then, its evolution stops to be recorded. Figure 3.4 shows for filaments created and their evolution.

The next step is to implement the computation of the best values of the free parameters in equations 3.2 and 3.3. The way I did it was by running the simulation several times or iterations. For each individual iteration with a given set of parameters, I made the same study described in section 2.7. In the end, I calculated the average and standard deviation for each bin of the histogram of orientation distributed by "octants" and compared this simulated data with observable data. If all observed data are inside simulated data $\pm 2\sigma$ the values of parameters introduced are good. If this is not verified, the values of the parameters are changed by adding a fixed step of 0.1, and the process is repeated. If, in the end of the simulation I have never achieved to explain the observation with 95% confidence for all "octant" the set of parameters that achived the highest confidence is saved. The program is run to create 5000 initial filaments and the number of iterations is 50. The values of parameters obtained in this process are showed in table 3.1.

Figure 3.5 shows the flowchart of the simulator.

Note that in this simulation the existence of degeneracy of the parameters obtained is not studied and it can be possible the combination of other parameters values giving a good agreement to the observations.

Figure 3.6 shows the distribution function for initial orientation given by equation 3.2 and 3.3, and figure 3.7 is the NCDF of the functions 3.2 and 3.3. Figure 3.8 shows the final result of the simulation.

The determination of the distribution function for the filaments orienta-

Table 3.1: Parameters inside the equations 3.2 and 3.3 by this procedure that produce the best agreement between observed and simulated data.

	values
a_1	1.0
b_1	1.5
c_1	0.3
d_1	0.7
a_2	0.1
b_2	2.0
c_2	0.1

tion is the most complicated part of this simulation,due to the CPU time that requires, because changes in any parameter or in the equation that I assume for this distribution, cause modifications in the final result. Figures 3.9 and 3.10 show the example of tested parameters that produced bad results.

The parameters used in the simulation that produce figure 3.9 are one example of the combination of parameters tested during the process to obtain the best combination of parameters. On table 3.2 are the differences in percentage of the parameter used in figure 3.8 and in figure 3.9.

Table 3.2: Differences in percentage of the parameter used in figure 3.8 and in figure 3.9.

	values
a_1	-90%
b_1	+25%
c_1	-96.66%
d_1	0%
a_2	+95%
b_2	+100%
c_2	+90%

From the approach used in this study it is not possible to do the same interpretation about how much changes in parameters changes the final result. In a future step, in parallel with the degeneracy of the parameters, these task can be implemented. In figure 3.10 we see the importance of the parameter d_1 in the final results.

Figure 3.11 shows how the perspective changes the observable orientation imposing a creation of the filaments with a single orientation.

From the analyses of figure 3.8 we can see that the distributions that the simulator creates are very close to the observations. Still, in some "octants" the observed distribution is not explained with 95% confidence by the simulation. This can be do to the differences between the observation and the simulations, for example in the inclinations close to the vertical, and because the observation distribution have a behavior like noise and same times a few point leave out of the interval of $\pm 2\sigma$.

Considering the approximations that I made in the simulation and all the effects that can introduce in the observed orientation, we saw that the perspective effect can explain the changes in the observed orientation distribution in the different "octants".

From the analysis of table 3.1, we see that in equation 3.2 the parameter related to the uniform distribution is much higher than in equation 3.3. This can be explained by the difference between the active region, where the configuration of the magnetic field is more irregular and can produce filaments more dispersed in orientation. On the contrary, in the quiescent zone the filaments appearance is dominated by the solar crow filaments channel [20].

In relation to the height and half width of the gaussian represented by equations 3.2 and 3.3 we see that in the quiescent zone the gaussian is more high and more narrow than the gaussian that fits the active zone behavior. This can be related to the same effect described for the uniform orientation parameter.

The final parameter is the amplitude and algebraic sign of the *sinus* curve in equation 3.2. In the beginning I expected based on the fact that filaments tend to appear approximately perpendicular to the magnetic field in active regions, that the filaments would have in the active region in the north hemisphere an initial orientation close to 85 degrees, because the average tilt of active regions varies between 0 and 10 degrees [3]. But I observed instead that the orientation distribution of filaments in the north hemisphere has a maximum at -40 degrees.

But if I consider that in many cases, the filaments are created in one

active region but are connected with filaments along for two or more active regions [21], it is easier to understand how we observe the maximum of the distribution at -40 degrees. In figure 3.12 we can see how the filaments connect between two active regions and how in this configuration the filaments appear with an orientation close to that observed in the simulation.

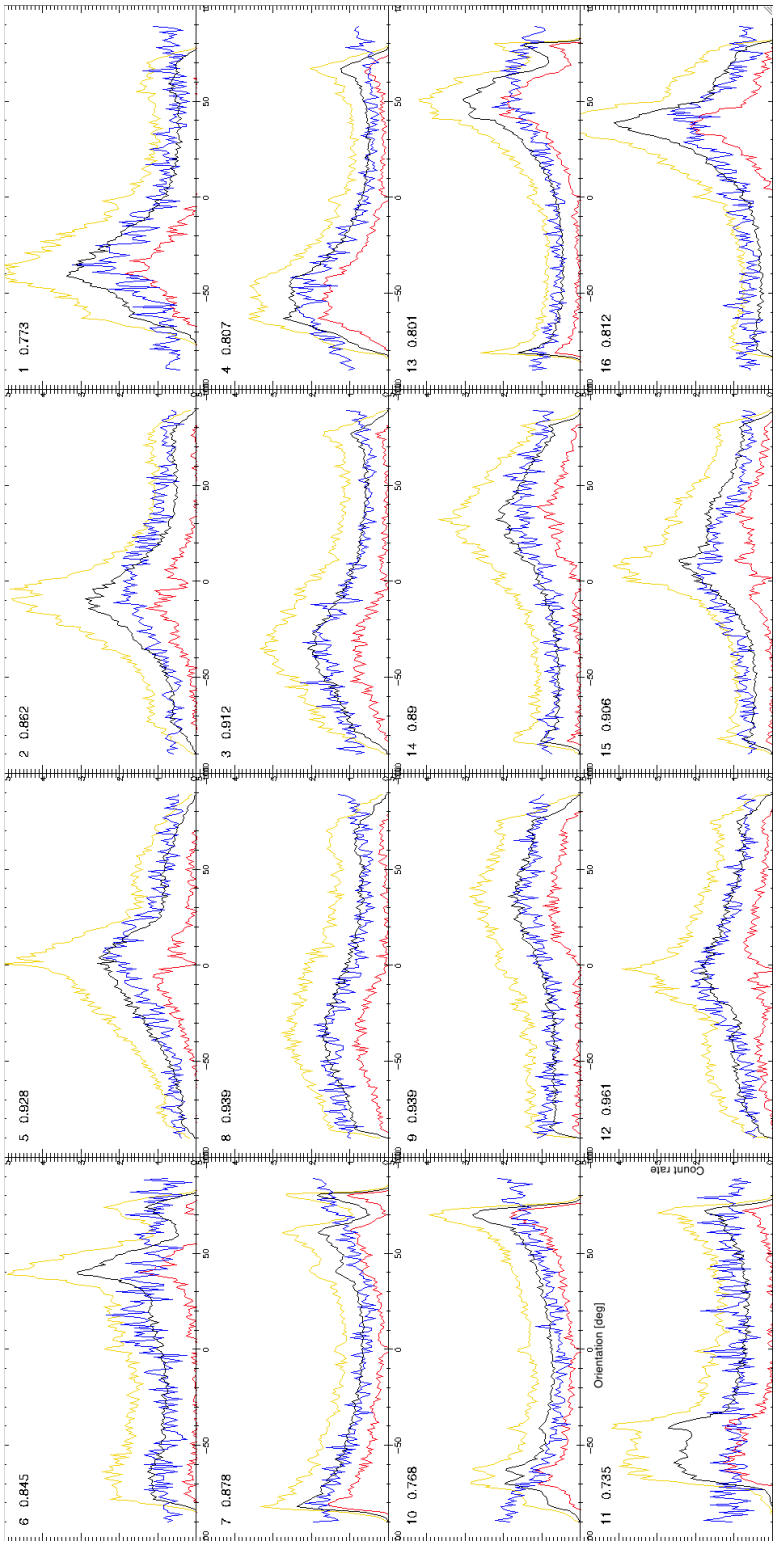

Figure 3.3: Example of the results obtained when the *sinus* shape are considered and using the parameters values of table 3.1. The blue line is the observable data, the black line is the result of the simulation and yellow and red lines are the simulation result$\pm$ 2σ.

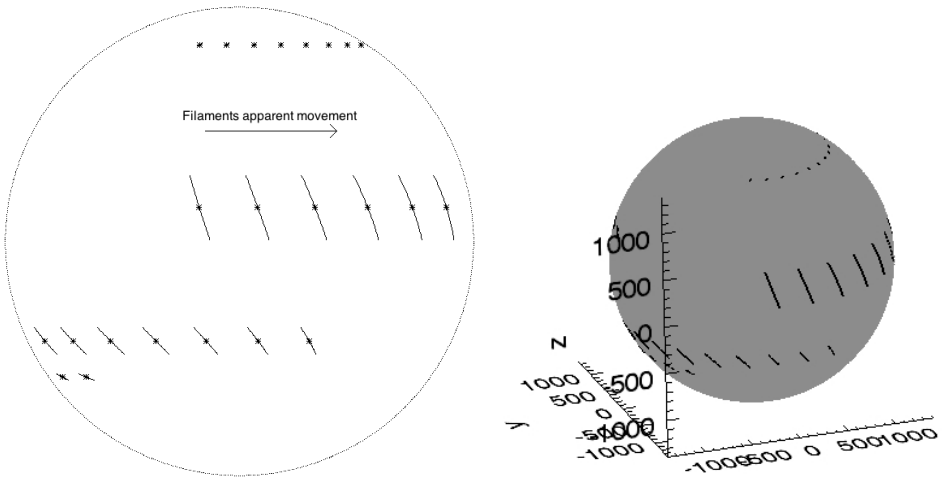

Figure 3.4: Example of the evolution in time of four simulated filaments.

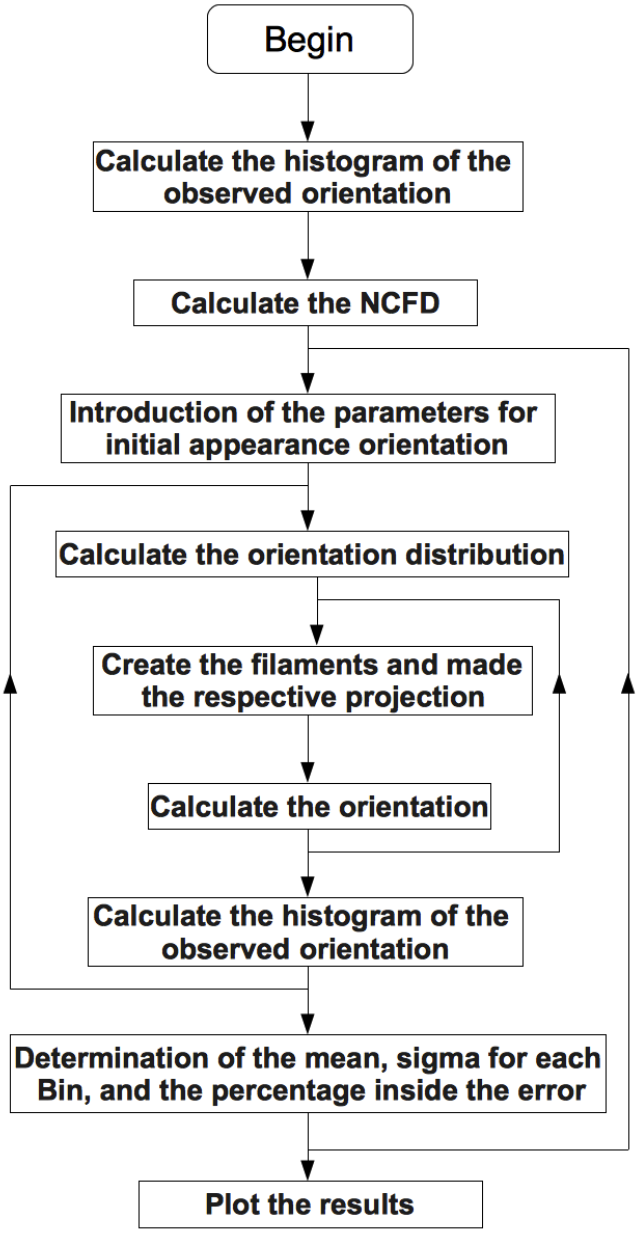

Figure 3.5: Flowchart of the simulation program.

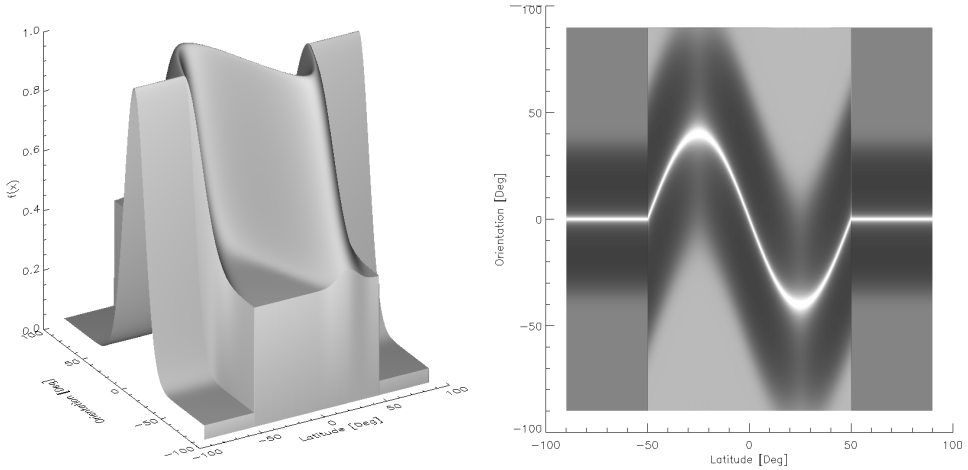

Figure 3.6: Distribution of initial orientation distribution obtained using the parameters inside the table 3.1. Right panel is the lateral view and the left panel is the top view.

.

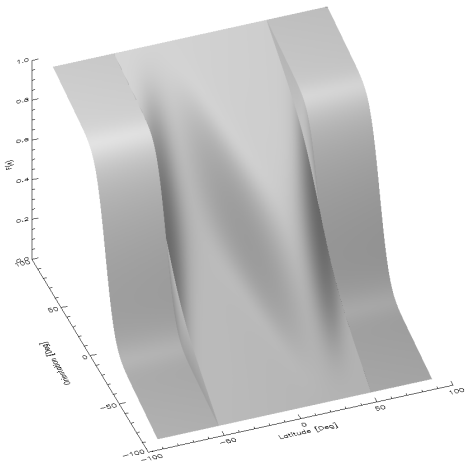

Figure 3.7: NCDF of initial orientation distribution showed in figure 3.6.

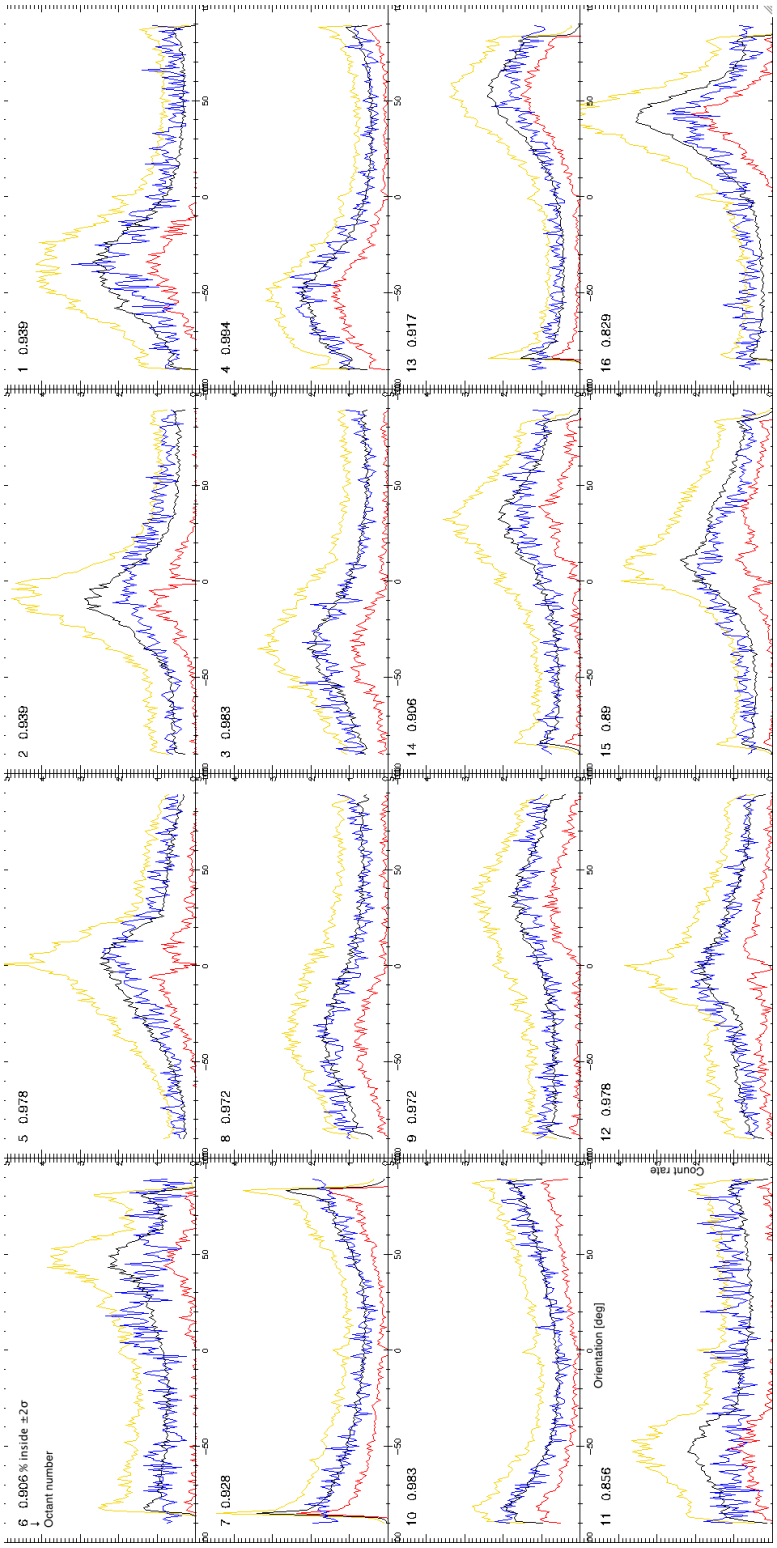

Figure 3.8: Results of the simulation obtained using the parameters inside the table 3.1. The blue line is the observed result the black line the result of the simulation and yellow and red lines are the simulation result± 2σ.

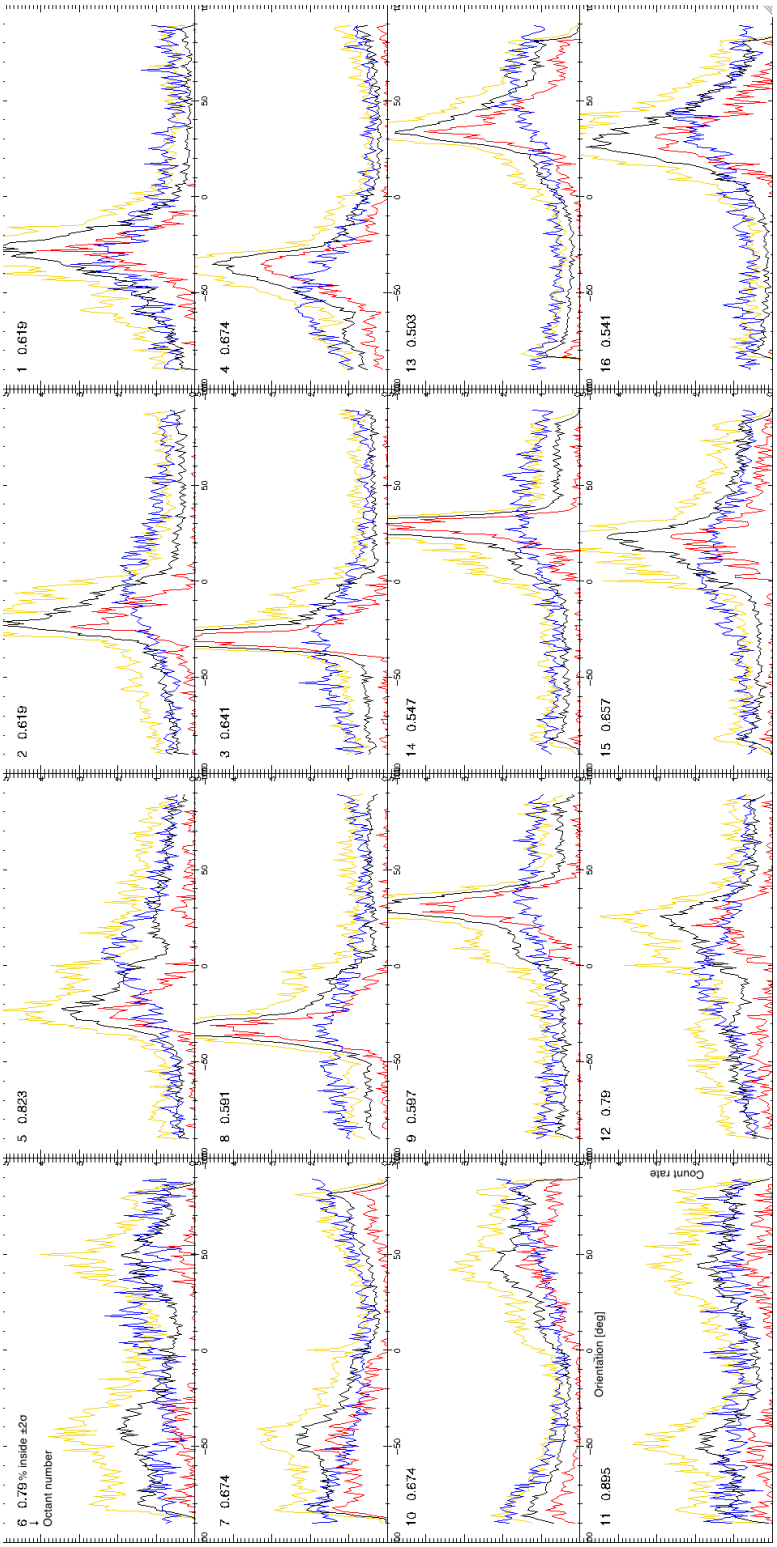

Figure 3.9: Example of parameters that produce bad results. a_1=0.1, b_1=2, c_1=0.01 , d_1=0.7, a_2=2, b_2=4, and c_2=0.01. The blue line is the observable result the black line the result of the simulation and yellow and red lines are the simulation result$\pm$ 2σ.

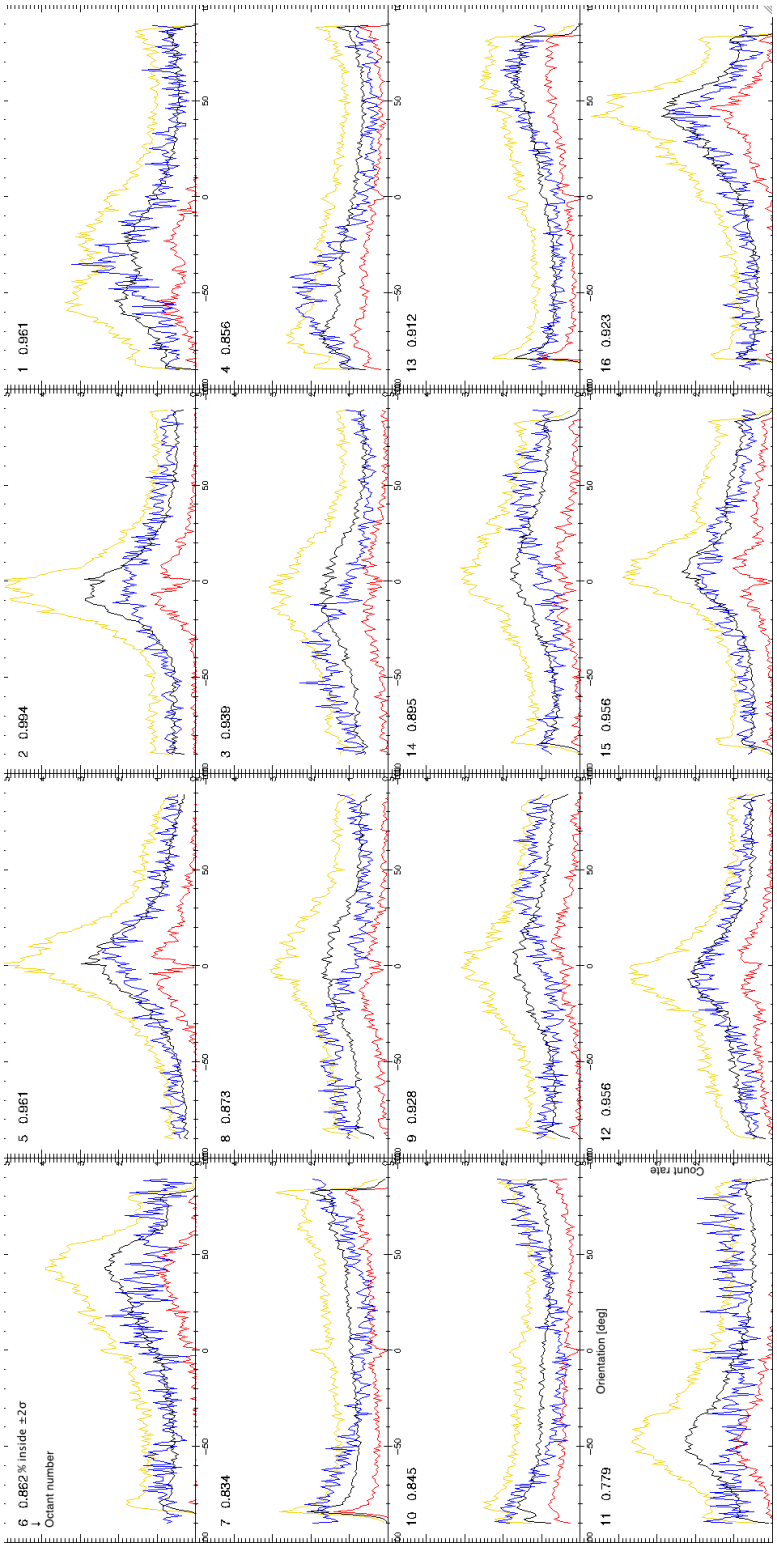

Figure 3.10: Result obtained using the parameter inside the table 3.1 except the parameter d wich is equal to 0. The blue line is the observable result the black line the result of the simulation and yellow and red lines are the simulation result$\pm$ 2σ.

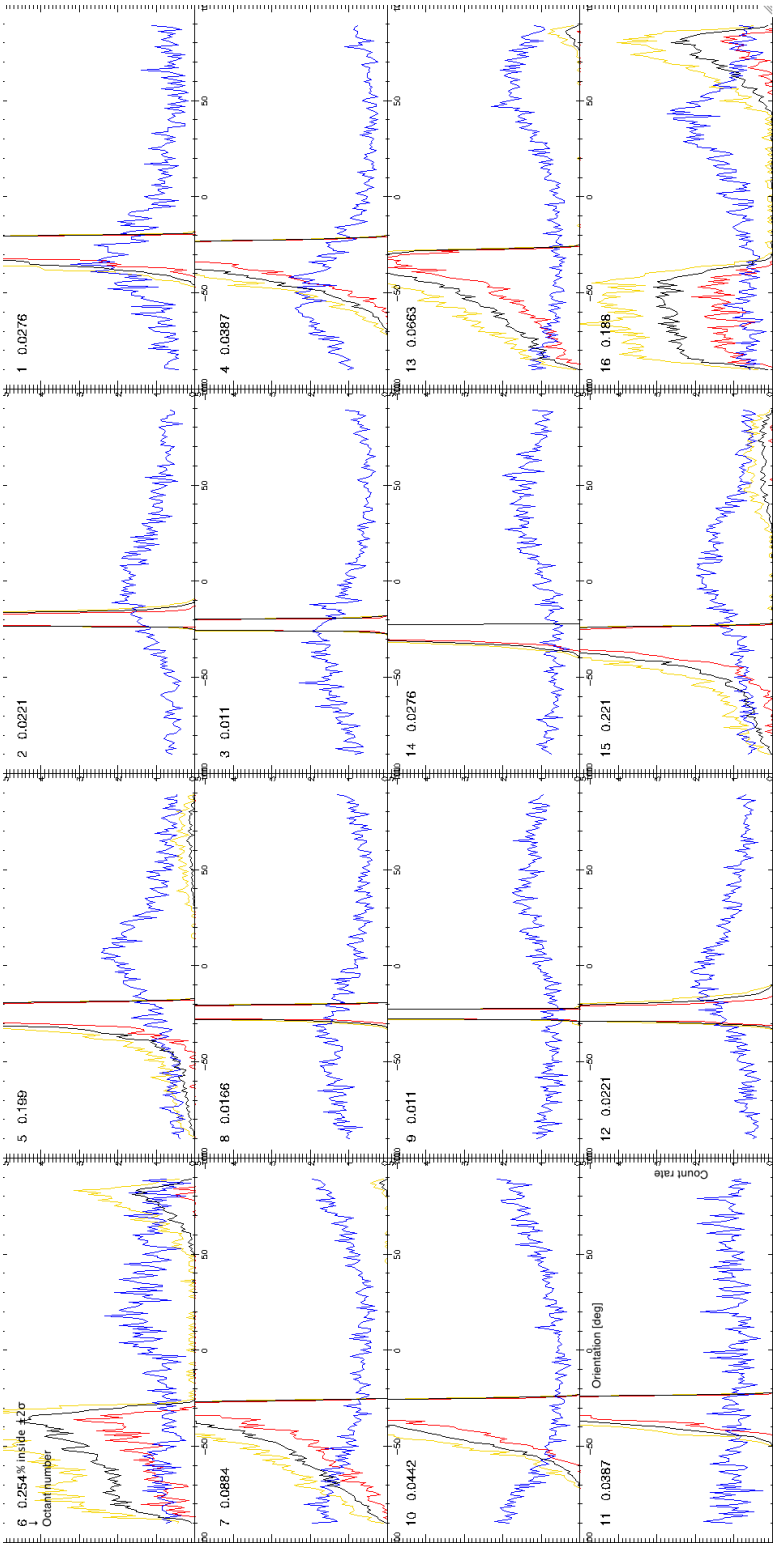

Figure 3.11: Example of the results obtained when we consider a criation of the filaments with a unique orientation $\pi/8$. The blue line is the observable result the black line the result of the simulation and yellow and red lines are the simulation result$\pm$ 2σ.

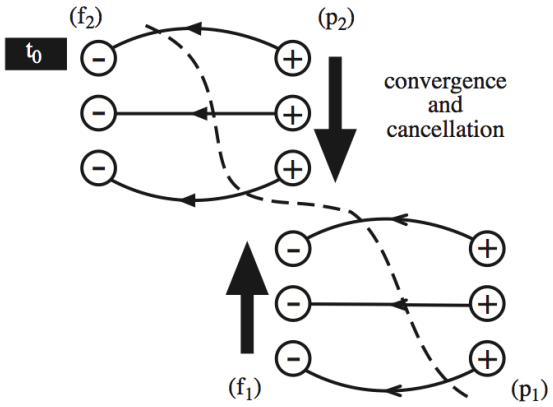

Figure 3.12: Example of the formation of the filaments between two active regions [21].

Chapter 4

Conclusion and perspectives

With the advancement on the computer programs available to scientists, it's now possible to treat long series of observational data. This applies to the data in the HFC database. In the case of this study it is provided for the, first time, the global data of one solar cycle in particularly the curvature, the orientation, the length and the location of solar filaments.

These new data allows new studies and new problems. In chapters 2 and 3 I present a statistical study of the different characteristics of filaments and a simulator that make possible an interpretation of the observations. I this conclusion I make a global synthesis, envisaging to draw some guidelines emerging from the current work.

In chapter 2 we saw that the filaments are distributed uniformly along the Carrington longitude. I obtaine the Carrington latitude distribution function for the appearance of filaments when the whole cycle is considered. I study the drift of the filaments along the Carrington latitude and (during the evolution of the cycle) I observe a derivation of the filaments from high latitudes towards the equator. I observe also the oscillation of approximately one year period behavior superimposed to the global linear drift in the ascending phase of the solar cycle of the sun. Until now I don't find I any explanation for this.

On the other hand I obtain the distribution of length of the filaments and I conclude that the existence of very long filaments ($> 60\ deg$ or $3.64 \times 10^5\ km$)

is very rare and the most frequent length of filaments is close to 2 deg or 1.21×10^4 km.

Concerning the filaments curvature I obtain the distribution for the curvature index for the whole cycle and I verify that this distribution can by a exponential distribution decay. More over, I observe an oscillation behavior of the rate of the exponential decay along the solar cycle that can be related to the turbulence of the magnetic field lines on the sun surface.

We verify that the position of active filaments lies between -50 and 50 deg. On the other hand the quiescent filaments appears outside of this regions.

The last statistical study and the most difficult to explain was related to the observed orientation of the filaments. In this statistical study I identified the difference in the observed orientation distribution between the central and the left and right "octants". But only based on a rough visual analysis, it is difficult identify the different possible effects that could be responsible for this behavior (eg. perspective). For this study, I felt the need to create a simulator.

By the analysis the results of the simulations, I can conclude that the perspective effect can be responsible for the behavior in the observable orientation. This takes in to account some hypothesis, namely the longitude and latitude appearance of the filaments skeleton center, the filament length, and the differential rotation.

Finally, concerning the approximations and the parameters introduced in the simulation, I checked that changes in the lifetime of the filaments, relative to the 10 days value, has a small impact in the final result.

For future work I plan to introduce distribution function for the lifetimes of the filaments, using the tracking information in the HFC database. The other parameter that can be taken into account in the simulation is the curvature of the filaments. The introduction of these two new elements in the simulation, is expectable to change the values of the parameters showed in table 3.1 and it can bring new interesting insights. One third improvement to be made is the introduction of time variation in the NCDF in the simulation. At this stage the simulation calculates the cycle as a whole and doesn't give any information about the time evolution of the filament behavior along the

cycle, except the evolution of the filaments lifetime. In order to provide a more realistic model of the filaments behavior we can use the studies made for the drift of the filaments and the curvature along the cycle.

Bibliography

[1] Paul. Murdin and Institute of Physics (Great Britain)). *Encyclopedia of astronomy and astrophysics / editor-in-chief Paul Murdin.* Nature Publishing Group, London, New York :, 2001.

[2] T. S. Wood and M. E. McIntyre. Polar confinement of the Sun's interior magnetic field by laminar magnetostrophic flow. *ArXiv e-prints*, May 2010.

[3] M. Dasi-Espuig, S. K. Solanki, N. A. Krivova, R. Cameron, and T. Peñuela. Sunspot group tilt angles and the strength of the solar cycle. *Astronomy & Astrophysics*, 518:A7, July 2010.

[4] E.R.Priest. *Dynamics and Structure of Quiescent Solat Prominences.* Kluwer Academic Publishers, 1989.

[5] E. Priest. Magnetic structure of prominences. In V. Ruzdjak and E. Tandberg-Hanssen, editors, *Dynamics of Quiescent Prominences*, volume 363 of *Lecture Notes in Physics*, pages 150–186. Springer Berlin / Heidelberg, 1990. 10.1007/BFb0025648.

[6] E.R.Priest. *Solar Magnetohydrodynamics.* D. Reidel Publishing Company, 1984.

[7] P.A. Davidson. *An Introduction to Magnetohydrodynamics.* Cambridge University Press, 2001.

[8] S. Ipson, V. Zharkova, S. Zharkov, A. Benkhalil, J. Aboudarham, and N. Fuller. Automated technique for comparison of magnetic field inver-

sion lines with filament skeletons from the solar feature catalogue. *Solar Physics*, 228:399–421, 2005. 10.1007/s11207-005-6878-2.

[9] T. Amari, J. F. Luciani, Z. Mikic, and J. Linker. A twisted flux rope model for coronal mass ejections and two-ribbon flares. *The Astrophysical Journal Letters*, 529(1):L49, 2000.

[10] S. F. Martin. Conditions for the Formation and Maintenance of Filaments (Invited Review). *Solar Physics*, 182:107–137, September 1998.

[11] Ian. Ridpath and Oxford University Press. *A dictionary of astronomy [electronic resource] / [edited by] Ian Ridpath.* Oxford University Press, [Oxford] :, 2nd ed. edition, 2007.

[12] M. Klvaňa, A. Garcia, and V. Bumba. The Modernized Spectroheliograph at Coimbra. 368:549, May 2007.

[13] N. Fuller, J. Aboudarham, and R. D. Bentley. Filament Recognition and Image Cleaning on Meudon Hα Spectroheliograms. *Solar Physics*, 227:61–73, March 2005.

[14] V. V. Zharkova, S. S. Ipson, S. I. Zharkov, A. Benkhalil, J. Aboudarham, and R. D. Bentley. A full-disk image standardisation of the synoptic solar observations at the Meudon Observatory. *Solar Physics*, 214:89–105, May 2003.

[15] R. D. Bentley, A. Csillaghy, J. Aboudarham, C. Jacquey, M. A. Hapgood, K. Bocchialini, M. Messerotti, J. Brooke, P. Gallagher, P. Fox, N. Hurlburt, D. A. Roberts, and L. S. Duarte. HELIO: The Heliophysics Integrated Observatory. *Advances in Space Research*, 47:2235–2239, June 2011.

[16] A. Goel and A. R. Choudhuri. The hemispheric asymmetry of solar activity during the last century and the solar dynamo. *Research in Astronomy and Astrophysics*, 9:115–126, January 2009.

[17] S. F. Martin, R. Bilimoria, and P. W. Tracadas. Magnetic field configurations basic to filament channels and filaments. In R. J. Rutten & C. J. Schrijver, editor, *Solar Surface Magnetism*, page 303, 1994.

[18] John G. Beck. A comparison of differential rotation measurements (Invited Review). *Solar Physics*, 191:47–70, 2000. 10.1023/A:1005226402796.

[19] S. K. Park and K. W. Miller. Random number generators: good ones are hard to find. *Commun. ACM*, 31:1192–1201, October 1988.

[20] R. Hansen and S. Hansen. Global distribution of filaments during solar cycle No. 20. *Solar Physics*, 44:225–230, September 1975.

[21] Petrus C. Martens and Cornelis Zwaan. Origin and evolution of filament-prominence systems. *The Astrophysical Journal*, 558(2):872, 2001.